

RESEARCH ARTICLE

10.1029/2020JD034358

This article is a companion to Smith et al. (2021), <https://doi.org/10.1029/2020JD034341>

Key Points:

- The approximations and uncertainties in deriving airborne chemical observation-based tropospheric transit time distributions are examined
- The necessary approximation of trace gas lifetimes is found to be the largest source of uncertainty
- The method successfully identified a range of dynamical transport variability from aircraft measurements

Supporting Information:

Supporting Information may be found in the online version of this article.

Correspondence to:

L. L. Pan,
liwen@ucar.edu

Citation:

Chelpon, S. M., Pan, L. L., Luo, Z. J., Atlas, E. L., Honomichl, S. B., Smith, W. P., et al. (2021). Deriving tropospheric transit time distributions using airborne trace gas measurements: Uncertainty and information content. *Journal of Geophysical Research: Atmospheres*, 126, e2020JD034358. <https://doi.org/10.1029/2020JD034358>

Received 4 DEC 2020
Accepted 30 JUL 2021

Author Contributions:

Conceptualization: Sofia M. Chelpon, Laura L. Pan, Zhengzhao J. Luo, Elliot L. Atlas


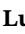




Data curation: Eric C. Apel, Rebecca S. Hornbrook

Formal analysis: Sofia M. Chelpon, Elliot L. Atlas, Kirk Ullmann, Samuel R. Hall

Investigation: Sofia M. Chelpon, Laura L. Pan, Zhengzhao J. Luo, Elliot L. Atlas, Warren P. Smith, Siyuan Wang, Kirk Ullmann, Samuel R. Hall, Eric C. Apel, Rebecca S. Hornbrook

© 2021. American Geophysical Union.
All Rights Reserved.

Deriving Tropospheric Transit Time Distributions Using Airborne Trace Gas Measurements: Uncertainty and Information Content

Sofia M. Chelpon¹ , Laura L. Pan² , Zhengzhao J. Luo³ , Elliot L. Atlas⁴ , Shawn B. Honomichl² , Warren P. Smith² , Siyuan Wang^{2,5} , Kirk Ullmann² , Samuel R. Hall² , Eric C. Apel² , and Rebecca S. Hornbrook² 

¹City University of New York Graduate Center, New York, NY, USA, ²Atmospheric Chemistry Observations and Modeling Laboratory, National Center for Atmospheric Research, Boulder, CO, USA, ³City University of New York City College, New York, NY, USA, ⁴University of Miami, Miami, FL, USA, ⁵Now at National Oceanic and Atmospheric Administration (NOAA) Chemical Sciences Laboratory (CSL), Cooperative Institute for Research in Environmental Sciences (CIRES), University of Colorado, Boulder, CO, USA

Abstract This study investigates the use of airborne in situ measurements to derive transit time distributions (TTD) from the boundary layer (BL) to the upper troposphere (UT) over the highly convective tropical western Pacific (TWP). The feasibility of this method is demonstrated using 42 volatile organic compounds (VOCs) measured during the Convective Transport of Active Species in the Tropics (CONTRAST) experiment. Two important approximations necessary for the application are the constant chemical lifetimes for each compound and the representation of the BL source by the local CONTRAST data. To characterize uncertainties associated with the first approximation, we quantify the changes in derived TTDs when chemical lifetimes are estimated using conditions of the BL, UT, and tropospheric average. With the support of a trajectory model study in a companion paper, we characterize the BL source region contributing to the transport to the sampled UT. In addition to the TTDs derived using a regional average, we analyze the potential information content in locally averaged measurements to represent the dynamical variability of the region. Around 150 TTDs, derived using measurements on a ~100 km spatial scale, show a distribution of mean and mode transit times consistent with the wide range of convective conditions encountered during the campaign. Two extreme cases, with the shortest and the near-longest TTD, are examined using the dynamical background of the measurements and back trajectory analyses. The result provides physical consistency supporting the hypothesis that sufficient information can be obtained from measurements to resolve dynamical variability of the region.

Plain Language Summary In this study, we use measurements of the atmospheric chemical composition to derive vertical transport timescales over the tropical western Pacific, where convective processes dominate. A large suite of trace gases with a wide range of chemical lifetimes are measured from a research aircraft. The trace gas measurements are used to construct “transit time distributions,” which capture the relative contributions of various transport pathways to the chemical composition of the upper troposphere in the study region. Results highlight the wealth of information in atmospheric chemical composition measurements, which is important not only for understanding chemistry of the atmosphere but also for quantifying aspects of atmospheric dynamics and circulation.

1. Introduction

Transport of trace gases in the atmosphere is a key process that links atmospheric chemical composition to weather and climate. Representing the transport processes in numerical models, together with emission rates and chemical transformation, is essential for understanding and predicting composition changes. Over the past several decades, the concept of the transit time distribution (TTD) has been established as an effective metric to characterize transport, and to bridge observations and models (Hall & Plumb, 1994; Holzer & Hall, 2000; Waugh & Hall, 2002). The TTD framework has had successful applications in stratospheric circulation and transport research, where the TTD is termed the “age spectrum.” The “Age of Air (AoA)” is a well-established diagnostic for stratospheric circulation. Characterization of mean age structure is a

Methodology: Sofia M. Chelpon, Laura L. Pan, Zhengzhao J. Luo, Elliot L. Atlas, Shawn B. Honomichl

Resources: Laura L. Pan, Zhengzhao J. Luo, Elliot L. Atlas, Shawn B. Honomichl

Software: Sofia M. Chelpon, Shawn B. Honomichl

Supervision: Laura L. Pan, Zhengzhao J. Luo

Validation: Warren P. Smith

Visualization: Sofia M. Chelpon, Shawn B. Honomichl, Warren P. Smith, Siyuan Wang

Writing – original draft: Sofia M. Chelpon

Writing – review & editing: Sofia M. Chelpon, Laura L. Pan, Zhengzhao J. Luo, Elliot L. Atlas, Siyuan Wang, Kirk Ullmann, Samuel R. Hall, Eric C. Apel, Rebecca S. Hornbrook

standard tool for model evaluations in stratospheric transport (e.g., Eyring et al., 2006; Ploeger et al., 2015; Schoeberl et al., 2003; Waugh, 2009; Waugh & Hall, 2002).

Developing AOA for diagnosing tropospheric transport is much more challenging. Stratospheric transport is dominated by the large-scale Brewer-Dobson circulation. In contrast, transport in the troposphere is determined by dynamical processes of a large range of spatial and temporal scales. More importantly, air enters the stratosphere primarily from the tropical tropopause, which makes it possible for the stratospheric mean AoA to be represented by a simple two-dimensional pattern (e.g., Figure 7 in Waugh & Hall, 2002), and the transport can be approximated as quasi-one-dimensional (Ehhalt et al., 2007; Hall & Plumb, 1994; Schoeberl et al., 2000, 2005). Tropospheric air masses, however, have many potential sources with different trace gas emission signatures. In addition, in the UTLS region, there can be contributions from distinct southern versus northern hemispheric surface boundary conditions from below, and there is also contribution from aged stratospheric air from above. This complexity makes it difficult to define a universal tropospheric AoA. The TTD diagnostics for the tropospheric transport have often been designed for specific source regions or to identify air mass origins for receptor regions of interest (e.g., Orbe et al., 2013; 2016; Waugh et al., 2013).

Although the stratospheric AoA has become a standard diagnostic using trace gas observations, such as SF₆, CO₂, N₂O, CH₄, and CFCs (e.g., Boering et al., 1996; Engel et al., 2009; Stiller et al., 2008; 2012), it is more difficult to derive an age spectrum using purely observations (e.g., Andrews et al., 1999; 2001; Ehhalt et al., 2007; Hauck et al., 2020). Similarly, few studies exist for deriving tropospheric TTD using observations (Holzer & Waugh, 2015; Luo et al., 2018). Most often the TTD diagnostics, which use the mathematical approach of the Green's function, are constructed using models, either facilitated by modeled chemical tracers, idealized radioactive tracers, or using pulse tracers representing surface emissions in Eulerian models (e.g., Haine & Hall, 2002; Holzer & Hall, 2000; Li et al., 2012; Orbe et al., 2013; 2016; Podglajen & Ploeger, 2019; Schoeberl et al., 2000, 2005; Waugh & Hall, 2002; Wu et al., 2020). A TTD (or Green's function) can also be derived using Lagrangian trajectory models (e.g., Bergman et al., 2013; Bowman & Carrie, 2002; Honomichl & Pan, 2020; Schoeberl et al., 2000).

In this work, we examine the approximations made in the approach of deriving TTD using airborne VOC measurements over the tropical western Pacific (TWP), following the feasibility study described in Luo et al. (2018). Scientifically, this development is motivated by the challenge of representing convection and convective transport in models, especially in hydrostatic global chemistry climate models. Convective transport is driven by processes that are often in “sub-grid” scale for global models. Convective parameterizations must be utilized to represent these processes, and doing so with reasonable accuracy has remained a significant challenge (Arakawa, 2004; Orbe et al., 2018). The airborne measurements from the Convective Transport of Active Species in the Tropics (CONTRAST) experiment of 2014 (Pan et al., 2017) provide an opportunity to develop an observation-based TTD diagnostic for characterizing convective transport. Using the NCAR Gulfstream V (GV) research aircraft, the campaign obtained ~100 vertical profiles from the sea surface to near 15 km measuring a large set of VOCs with chemical lifetimes ranging from hours to multiple decades. The range of lifetimes covered by these measurements enables the construction of TTDs from oceanic boundary layer (BL) to the layer of convective outflow in the upper troposphere (UT) following the specific approach of stratospheric age spectrum calculations in Schoeberl et al. (2005) and Ehhalt et al. (2007). Using this approach, the age spectrum is derived using modeled or observed chemistry trace gases of different lifetimes and the analytical form of the Green's function for the one-dimensional diffusion equation (Hall & Plumb, 1994).

To support this chemical-observation based TTD approach, we have conducted a companion study using Lagrangian backward trajectory calculations to construct TTD for the sampling locations of the chemical measurements (Smith et al., 2021 companion paper in the same issue, hereinafter referred to as WPS21). Specifically, the trajectory model analysis provides information on the limitations of the campaign measurements in representing the source of transport (Section 6). Additionally, we use these trajectory calculations to demonstrate the dynamical variability represented in the airborne samples (Section 7). Further, the application of the chemical-observation based TTD as a transport diagnostic is demonstrated in the comparison with the trajectory-based TTD (WPS21).

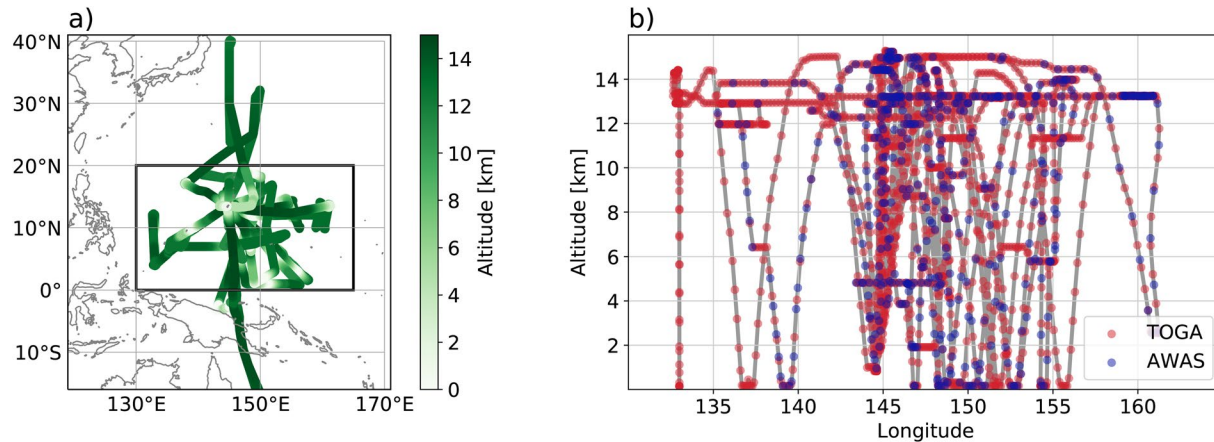


Figure 1. (a) Map of Convective Transport of Active Species in the Tropics GV flight tracks for relevant flights, colored by flight altitude. Box (130°–165°E, 0°–20°N) indicates the domain of the data used in this study. (b) Flight tracks in longitude-altitude cross section showing the vertical extent of the measurements used. Colored markers along the flight tracks indicate the position of Trace Organic Gas Analyzer (red) and Advanced Whole Air Sampler (blue) measurements.

Airborne field campaigns in the past two decades have accumulated a large suite of measurements of different trace gases that cover a wide range of photochemical lifetimes. The broader objective of this work is to explore the wealth of tropospheric transport information from these campaign data. A robust observation-based metric of transport such as the TTD is useful not only for evaluating transport processes in various models—in particular global chemistry climate models—but also for quantifying regional dynamical behavior that aids in the interpretation and analysis of trace gas measurements in different field campaigns.

2. The Approach and Approximations for Deriving the Chemical Observation-Based Tropospheric Transit Time Distribution

Our approach of deriving a TTD using airborne in-situ measurements of VOCs was foremost inspired by the measurements from the CONTRAST airborne campaign. The data showed a compact relationship between the BL-normalized UT VOC concentrations and their chemical lifetimes when averaged using all samples collected in the TWP domain (Luo et al., 2018). The compact relationship of campaign average data suggests that (a) treating the transport as in a steady state and considering the species lifetimes as constant within this layer of transport are reasonable approximations and (b) considering the UT layer (centered at a selected altitude z) over the campaign domain (0°–20°N, 130°–165°E, see Figure 1) as the target of transport and the BL layer (0–2 km) in the same domain as the source of the transport, we have essentially reduced the problem to a one-dimensional system. Under these approximations, the procedure to extract the TTD over the TWP from airborne trace gas measurements follows closely that described in Schoeberl et al. (2005) and Ehhalt et al. (2007) for deriving stratospheric age spectrum with applications of the one-dimensional diffusion equation from Hall and Plumb (1994).

Specifically, we consider the following equation relating the mixing ratio of target layer, $m_{is}(z)$, to that of the source layer at $z_0 = 0$, m_{io} :

$$m_{is}(z) = m_{io} \int_0^{\infty} e^{-t/\tau_i} G(z, t) dt, \quad (1)$$

where $G(z, t)$ is the Green's function representing the TTD at the UT layer (target) centered on altitude z , t is the transport time, and τ_i is a constant chemical lifetime for species i as presented in Table 1. The Green's function, G , is in general a function of space and time coordinates of both source and target points. It is simplified here to only depend on target point height and time, $G(z, t)$, when the source is approximated as a single BL layer average at altitude $z_0 = 0$, and the transport initial time is set to $t_0 = 0$ under a steady state approximation (Ehhalt et al., 2007; Hall & Plumb, 1994; Schoeberl et al., 2005). This equation is further simplified if we normalize the target layer mixing ratio of a trace gas by its mixing ratio at the source:

Table 1

Lifetimes of Selected Volatile Organic Compounds Observed During CONTRAST by the Trace Organic Gas Analyzer (TOGA) and Advanced Whole Air Sampler (AWAS) Instruments

Trace gas	Chemical formula	Instrument	τ_{BL} (day)	τ_{TROPO} (day)	τ_{UT} (day)	Source of estimate
Acetaldehyde ^a	C ₂ H ₄ O	TOGA	0.28	0.32	0.35	Calculated
Dimethyl Sulfide	C ₂ H ₆ S	AWAS	0.66	0.38	0.41	Calculated
n-Pentane	C ₅ H ₁₂	AWAS	1.2	2.4	4.7	Calculated
n-Butyl Nitrate ^a	C ₄ H ₉ NO ₃	AWAS	2.2	3.1	4.1	Calculated
n-Butane	C ₄ H ₁₀	TOGA, AWAS	2.0	3.9	8.1	Calculated
Isobutane	C ₄ H ₁₀	TOGA, AWAS	2.2	4.1	7.9	Calculated
2-Butyl Nitrate ^a	C ₄ H ₉ NO ₃	AWAS	3.8	4.8	5.5	Calculated
Benzene	C ₆ H ₆	TOGA, AWAS	3.8	6.6	12	Calculated
Isopropyl Nitrate ^a	C ₃ H ₇ NO ₃	AWAS	6.7	7.9	8.8	Calculated
Propane	C ₃ H ₈	TOGA, AWAS	4.3	9.4	23	Calculated
Methanol	CH ₄ O	TOGA	5.2	9.8	20	Calculated
Ethyne	C ₂ H ₂	AWAS	5.5	9.8	19	Calculated
Chlorobenzene	C ₆ H ₅ Cl	AWAS	8.0	10	14	Calculated
Ethyl Nitrate ^a	C ₂ H ₅ ONO ₂	AWAS	11	13	15	Calculated
Bromoform ^a	CHBr ₃	TOGA, AWAS	13	19	25	Calculated
Dibromochloromethane	CHBr ₂ Cl	AWAS	13	24	46	Calculated
1,2-Dichloroethane	C ₂ H ₄ Cl ₂	AWAS	19	51	150	Calculated
Ethane	C ₂ H ₆	AWAS	19	52	170	Calculated
Bromodichloromethane	CHBrCl ₂	AWAS	28	57	130	Calculated
Tetrachloroethylene	C ₂ Cl ₄	TOGA, AWAS	28	83	320	Calculated
Dibromomethane	CH ₂ Br ₂	TOGA, AWAS	40	100	310	Calculated
Bromochloromethane	CH ₂ BrCl	AWAS	46	120	370	Calculated
Dichloromethane	CH ₂ Cl ₂	TOGA, AWAS	47	120	350	Calculated
Chloroform	CHCl ₃	TOGA, AWAS	48	120	370	Calculated
Methyl Chloride	CH ₃ Cl	AWAS	130	430	1,900	Calculated
Methyl Bromide	CH ₃ Br	AWAS	160	560	2,600	Calculated
Carbonyl Sulfide	OCS	AWAS	2,000	2,000	2,000	Johnson (1981)
HCFC-141b	CH ₃ CCl ₂ F	AWAS	840	3,300	19,000	Calculated
Methyl Chloroform	CH ₃ CCl ₃	AWAS	850	3,300	18,000	Calculated
HFC-365mfc	C ₄ H ₅ F ₅	AWAS	1,000	3,700	19,000	Calculated
HCFC-22	CHClF ₂	AWAS	1,100	4,500	26,000	Calculated
HCFC-142b	CH ₃ CClF ₂	AWAS	1,500	5,700	37,000	Calculated
Halon-1211	CBrClF ₂	AWAS	5,800	5,800	5,800	SPARC Report No. 6
HCFC-134a	CH ₂ FCF ₂	AWAS	1,500	6,300	37,000	Calculated
Halon-2402	CBrF ₄	AWAS	10,000	10,000	10,000	SPARC Report No. 6
Carbon Tetrachloride	CCl ₄	TOGA, AWAS	12,000	12,000	12,000	SPARC Report No. 6
CFC-112a	C ₂ Cl ₄ F ₂	AWAS	19,000	19,000	19,000	Carpenter et al. (2014)
CFC-11	CCl ₃ F	AWAS	19,000	19,000	19,000	SPARC Report No. 7

Table 1
Continued

Trace gas	Chemical formula	Instrument	τ_{BL} (day)	τ_{TROPO} (day)	τ_{UT} (day)	Source of estimate
CFC-112	C ₂ Cl ₄ F ₂	AWAS	22,000	22,000	22,000	Carpenter et al. (2014)
CFC-113	C ₂ Cl ₃ F ₃	AWAS	34,000	34,000	34,000	SPARC Report No. 6
CFC-12	CCl ₂ F ₂	AWAS	37,000	37,000	37,000	SPARC Report No. 6
CFC-114	C ₂ Cl ₂ F ₄	AWAS	69,000	69,000	69,000	SPARC Report No. 6

Note. Calculated τ_{BL} (~1 km), τ_{UT} (~13 km), and τ_{TROPO} (troposphere average) for the Convective Transport of Active Species in the Tropics (CONTRAST) study area. Two significant figures are kept for VOC lifetimes.

^aSpecies include photolysis loss in the lifetime calculation.

$$\mu_i(z) = \int_0^{\infty} e^{-t/\tau_i} G(z,t) dt, \quad (2)$$

where the normalized target layer mixing ratio, $\mu_i(z) = (m_{is}(z)/m_{io})$, is the Laplace transform of $G(z, t)$. Using the analytical form of $G(z, t)$ based on the one-dimensional diffusion equation (Ehhalt et al., 2007; Hall & Plumb, 1994; Schoeberl et al., 2000, 2005),

$$G(z,t) = \frac{z}{2\sqrt{\pi K t^3}} \exp\left(\frac{z}{2H} - \frac{Kt}{4H^2} - \frac{z^2}{4Kt}\right), \quad (3)$$

where H is the scale height, and K is the diffusion coefficient. Following Ehhalt et al. (2007), we determine $G(z, t)$ using the constraint of airborne observations.

As described in Luo et al. (2018) we focus on a UT layer with an altitude range 12–14 km, with the height variable z assigned as 13 km, the midpoint of the layer. This leaves the target time t as the only variable in the Green's function, $G(t)$. To determine the TTD for the UT layer, the scale height, H , is chosen to be 7.6 km, estimated using a layer-averaged temperature of approximately 260 K. The diffusion coefficient K is numerically determined via regression by minimizing the cost function F :

$$F = \sum_{i=1}^{52} (\mu_i - \mu_i^*)^2, \quad i = 1, 2, \dots, 52, \quad (4)$$

where μ_i is calculated from Equation 2 and μ_i^* represents the UT fraction of i th specie derived from measurements. Fifty-two independent measurements of 42 VOC species are used (Luo et al., 2018). The resulting $G(t)$ represents the chemical observation-based TTD. Mean and modal transit times are used to represent the time scale of the transport, with modal transit times being the time where $G(t)$ is maximized and mean transit times being the first moment of the distribution.

In a feasibility study, Luo et al. (2018) demonstrated the application of this approach to characterize tropospheric transport over the convectively active TWP. The resulting mean time scale of ~10 days for the UT layer of main convective outflow is consistent with the transit time estimated from convective mass flux of the region. However, the uncertainty of the calculation is not well understood. In particular, two key simplifying approximations are the use of a set of constant VOC lifetimes estimated using the BL conditions, and the use of BL measurements in the campaign domain as the transport initial conditions. The goal of the present work is to examine the sensitivities and uncertainties related to these approximations, as well as the information content represented in the locally averaged measurements. These developments will help interpret the results and to establish a quantitative diagnostic tool. In this work we address the following set of questions:

1. What is the range of uncertainty in the derived TTDs from using a constant lifetime to represent a range of lifetime variability throughout the layer of transport from the BL to UT? (Sections 4 and 6.1).
2. What is the estimated uncertainty from using BL samples measured during CONTRAST to represent the initial mixing ratios of trace gases transported to the UT? (Section 6.2).
3. CONTRAST airborne measurements sampled a wide range of dynamical conditions. Do the measurements from local segments contain sufficient information to derive physically meaningful TTDs to represent the transport variability in the region? (Section 7).

3. CONTRAST Experiment and Data Used

The CONTRAST campaign took place in January–February 2014 and was operated from Guam (13.4°N, 144.8°E). The experiment was primarily motivated by the need for a better understanding of trace-gas composition and transport in the highly convective TWP during boreal winter, the season of maximum convection in the region (Pan et al., 2017). The flight tracks of 12 research flights (RFs) of the GV research aircraft conducted from Guam are shown in Figure 1. Figure 1a shows the latitude-longitude extent of the sampling. Data used in this study are confined to the inset black box (130°–165°E, 0°–20°N) in Figure 1a. Because the focus of our study is on transport in the tropics, observations north of 20°N are not used. Data from RF06 are excluded as it targeted strong extratropical influence (Donets et al., 2018). Figure 1b shows the vertical sampling extent of the data used in this study. Approximately 100 vertical profiles were sampled, with the vertical range from 300 m above sea level (asl.) to the ceiling of the GV, ~15 km (Pan et al., 2017).

In this study, we choose to focus on a layer between 12 and 14 km, following Luo et al. (2018). This is the altitude range that covers most of the GV's high-altitude cruise-level legs, and it is within the altitude range of the main convective outflow indicated by both the airborne trace gas data and the satellite cloud distribution (Pan et al., 2017). The BL samples are selected to be within the layer 0–2 km above sea level (asl). For the purpose of this study, the BL is used to identify the chemical composition of the primary air mass which contributes to vertical convective transport. This is different from the traditional definition of the marine BL. Uncertainties related to the choice of BL are discussed in Section 6.2. BL samples collected within ~11 km of Guam are removed, as these can contain outliers representative of strong and localized anthropogenic pollution associated with the developed area.

Chemical data used in this study are measurements of the Trace Organic Gas Analyzer (TOGA) and Advanced Whole Air Sampler (AWAS) instruments; each samples a large suite of VOCs with lifetimes ranging from hours to decades. Sampling density and locations of TOGA and AWAS are marked on the flight tracks in Figure 1b. The TOGA instrument is an *in-situ* gas chromatograph/mass spectrometer. During CONTRAST, TOGA measured mixing ratios of VOCs approximately every two minutes, with a sample collection time of 35 s. Precision, accuracy, and detection limit are compound specific. TOGA is capable of measuring several oxygenated VOCs with short to intermediate atmospheric lifetimes that cannot be as reliably sampled using whole air canisters (Apel, 2014; Apel et al., 2015; Wang, Hornbrook, et al., 2019; Wang et al., 2020). The AWAS instrument has a lower spatial resolution than TOGA, but is capable of higher precision and can measure a larger suite of halocarbons, organic nitrates, and non-methane hydrocarbons. Sixty canister samples were collected per flight, with sampling times ranging from several seconds near the surface to ~40 s in the UT. Canisters were analyzed post-flight using a custom GC/MS/FID/ECD analytical system (Atlas, 2014; Donets et al., 2018). Sampling overlap between the two instruments allowed comparison of measurement data (Andrews et al., 2016; Atlas, 2014). For the 10 species for which measurements were collected from both TOGA and AWAS instruments, the results are consistent to within 1%–10% in the campaign average BL and UT layers for most species, with exceptions of Propane (~26% in BL) and Isobutane (~22% UT).

To derive TTDs in this region of intense convection, we selected 42 species for this analysis, shown in Table 1. Since there are 10 species sampled by both TOGA and AWAS, we have 52 independent trace gas measurements in the suite. Not all TOGA and AWAS species were included in the development of the TTD. We chose species which typically have maximum mixing ratios in the BL, and have no significant *in-situ* chemical production in the atmospheric column. Their concentrations in the free troposphere are controlled primarily by chemical loss and transport (including mixing) processes (see Section 5). We also include very long lifetime species such as CFCs. We recognize that some species included to characterize the shorter end of the transport spectrum have sources of *in-situ* production (acetaldehyde, methanol), but we have found that they do not introduce issues in the fitting. We have removed species with a strong oceanic sink, such as HCN, and species with significant reaction chemistry in the free troposphere, such as formaldehyde (Anderson et al., 2017; Singh et al., 2003). In addition, species with their UT mixing ratios frequently below the instrument detection limits were excluded.

To avoid a high bias in the mean mixing ratios, VOCs flagged as “below detection limit” are assigned a value empirically. For statistical averaging/analysis of species measured by TOGA, measurements

below detection limit are substituted with a value of half of that trace gas' detection limit (Cohen & Ryan, 1989). The fraction of TOGA samples in the UT and BL that consist of substituted values after this data treatment ranges from 0% (e.g., CH₂Br₂, CH₂Cl₂) to 43% (acetaldehyde). Means are calculated using trace gases for which we have >50% measurements above detection limit. AWAS detection limits vary with each species data collected per flight, so AWAS detection limits are estimated to be 80% of the lowest sample determined per trace gas, per flight. Only 4 AWAS species (DMS, 2-butyl nitrate, n-butyl nitrate, and CHBr₂Cl) were observed below the AWAS detection limit. Sensitivity tests for substituting data with below detection limit values showed that there is little impact on the resulting TTD mode or mean when the missing data are substituted by the detection limit value, half the detection limit value, or zero. However, omitting the below detection limit samples altogether skews mixing ratio means high.

4. Lifetimes of Selected VOCs

The *in-situ* VOC measurement-based TTD calculation is designed with an assumption that each species' chemical lifetime in the layer of atmosphere of interest can be approximated by a constant. Since chemical lifetimes depend on atmospheric conditions (Atkinson, 1986; Lu et al., 2012; Shetter et al., 2002), it is important to examine the range of parameters that impact chemical lifetimes in the atmospheric layer of interest. This information is a key step in assessing the impact of the lifetime uncertainty on the derived TTD.

Two primary sinks for VOCs in the troposphere are destruction by hydroxyl radical (OH) and photolysis decay (Lu et al., 2012; Shetter et al., 2002). These two factors are used to calculate approximate atmospheric lifetimes for the set of trace-gas species observed during the CONTRAST campaign (Table 1). Atmospheric lifetimes of several long-lived species are well-documented in the literature and so they are not calculated in this study (Carpenter et al., 2014; Johnson, 1981; Ko et al., 2013; Liang et al., 2016), as shown in the right-most column of Table 1.

Variables influencing chemical loss due to OH are temperature and OH concentration, both of which decrease from the BL to UT, on average. To assess how the lifetime of each trace gas might affect the TTD, we choose to calculate the lifetimes using three sets of temperature and OH concentrations that best represent the BL, UT, and tropospheric average. The temperature values are based on campaign average of the GV measurements, and Nicely et al. (2016) results provide the 24-h average OH concentrations which use the January–February CONTRAST campaign measurements as constraints. The results are denoted as τ_{BL} , τ_{UT} , and τ_{TROPO} . A brief description of the calculation is below. Additional details on lifetime calculations are provided in Appendix A. An assessment of how OH variability impacts approximated lifetimes and the resulting TTD are presented in Appendix B.

Atmospheric lifetimes due to OH reaction (τ_{OH}) and photolysis (τ_{photo}) are calculated separately, then combined to produce one representative total lifetime (τ) by Equation 5. Other sources of loss exist, shown by the residual term (τ_x), but are not considered in this study as we assume their contribution to the selected species to be relatively minor (Atkinson, 1986; Madronich, 1987). For example, trace gas losses due to halogen chemistry or deposition are not considered here.

$$\frac{1}{\tau} = \frac{1}{\tau_{OH}} + \frac{1}{\tau_{photo}} + \dots + \frac{1}{\tau_x} \quad (5)$$

Table 1 shows lifetimes from three sets of conditions, τ_{BL} , τ_{UT} , and τ_{TROPO} , calculated by combining τ_{OH} and τ_{photo} via Equation 5. As chemical loss rates vary following vertical gradients in temperature, OH concentration, and intensity of solar radiation, trace gas lifetimes generally increase with altitude. Lifetimes tend to be shortest in the BL and longest in the UT. The substantially longer UT lifetimes are due to the diminished OH and lower temperatures compared to the BL (Nicely et al., 2016). The largest differences in BL to UT lifetime occur in OH loss dominated species, such as HCFCs, methyl chloride, and methyl bromide. In the most extreme case for HCFC-142b, we observe a relative increase of ~2,400% from BL to UT lifetimes. The six species in this study that have significant photolysis loss

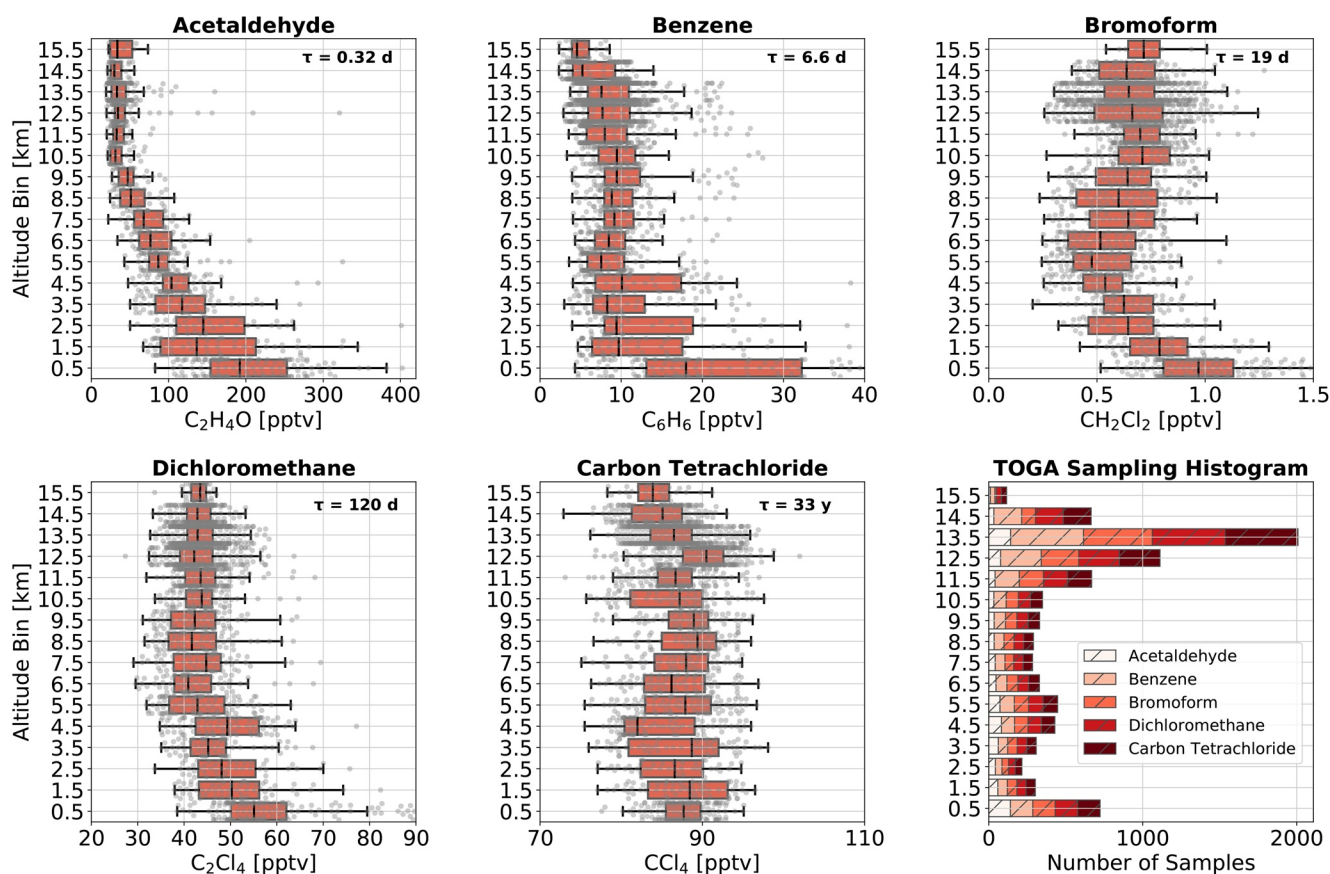


Figure 2. Vertical profiles for six selected trace gases sampled by Trace Organic Gas Analyzer (TOGA), arranged by increasing tropospheric lifetimes. Boxplots represent sampled distribution in each 1-km GPS altitude, and the gray scatter shows all samples. Boxes show the interquartile range (IQR), while whiskers correspond to 1.5 times the IQR of the data. The vertical sampling distribution for each TOGA measured trace gas is also shown.

tend to have the smallest difference in UT and BL lifetime, as the increase in photolysis loss due to increased radiation with altitude offsets the diminished OH loss (Dvorkin & Steinberger, 1999). For example, acetaldehyde has just a 23% increase in lifetime from the BL to the UT. The one exception to this is DMS, which sees a decrease in lifetime with altitude due to its O₂ dependence (Albu et al., 2006; Hynes et al., 1986; Williams et al., 2001).

5. Signature of Convective Transport in Vertical Profiles

A number of previous studies have demonstrated that the effect of convective transport is often revealed in trace gases' vertical profiles (e.g., Folkins & Martin, 2005; Pan et al., 2017). In this analysis, the changes in vertical structure of the profiles when arranged by species lifetimes provide a clear signature for convective transport. Binned vertical profiles for selected TOGA and AWAS measurements during CONTRAST are shown in Figures 2 and 3, where profiles of five species from each instrument are shown in both scatter and statistical distributions in 1-km altitude bins. The number of samples of each trace gas collected per 1-km layer are also shown in the figures. This set of profiles and the pattern of the progression in the vertical profiles demonstrate that the convective influence on the species' UT concentrations varies in accordance with the species' tropospheric lifetimes. These figures highlight the physical intuition for quantifying transport time scales using the relationship between the UT fractions and chemical lifetimes.

The examples in Figures 2 and 3 are selected to represent short-lived, intermediate, and long-lived species. The “short” to “long” in this case are relative to the convective transport time scales. What we consider as “short-lived” trace gases have lifetimes of hours up to a few days, and display maximum mixing ratios

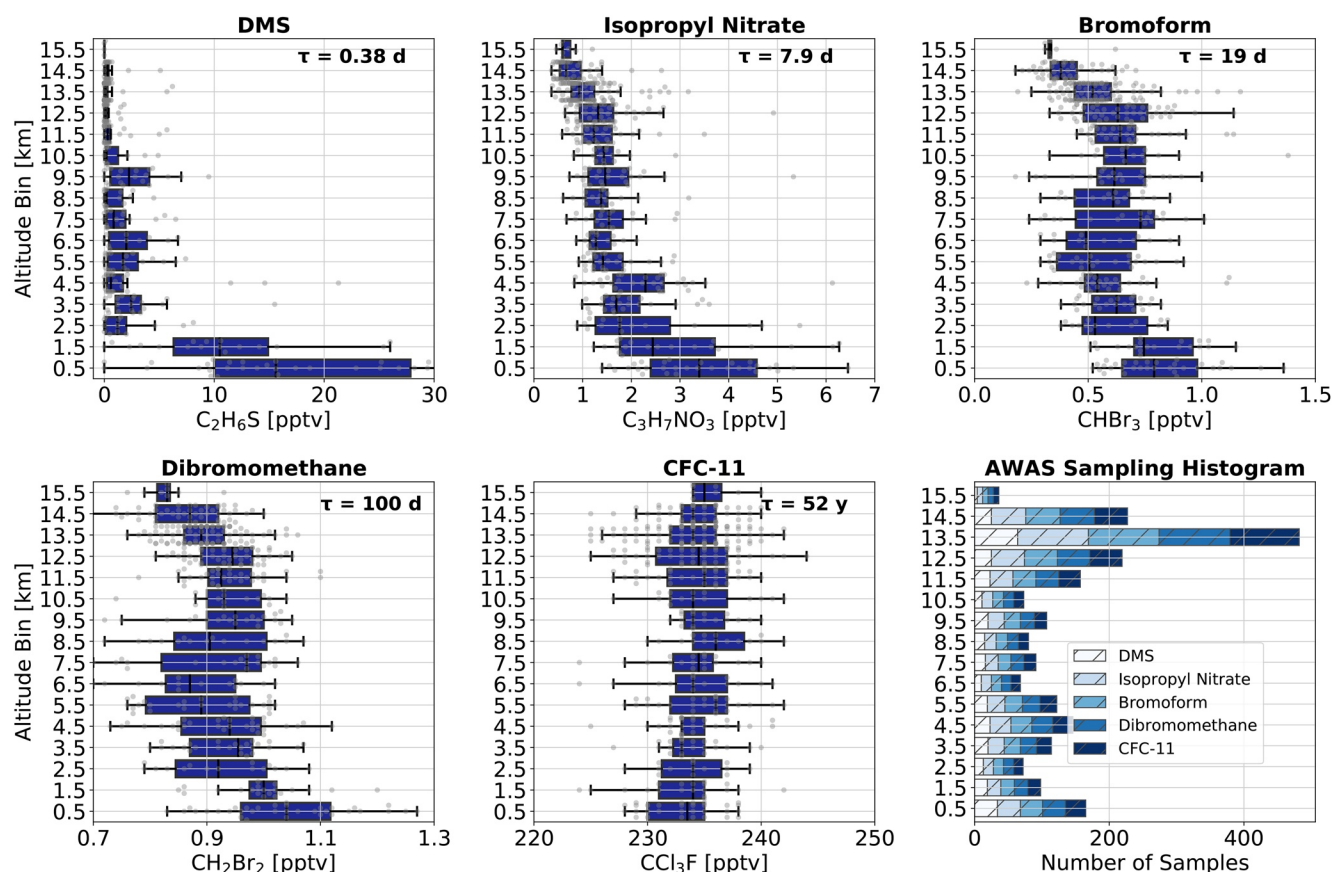


Figure 3. Same as Figure 2 but for six selected trace gases sampled by Advanced Whole Air Sampler.

in the BL with rapid decrease upwards into the UT. Two examples are acetaldehyde (Figure 2) and DMS (Figure 3). These species do not show significant enhancement in the UT on the regional scale. In sampling these species, oftentimes the UT concentrations fall below the instruments' detection limit in the UT. The observed UT enhancements are typically outliers directly related to fresh convective outflow and fast updrafts (Pan et al., 2017). Although only a few short-lived species are available in sufficient sampling, they play an important role in representing the short end of the TTD.

Species with what we call “intermediate” lifetimes survive for between a few weeks and 1 year, and these can be seen in bromoform (Figures 2 and 3), and isopropyl nitrate (Figure 3). The species' mixing ratios are consistently enhanced in the UT during CONTRAST. These species typically display a distinct reverse s-shaped vertical profile, showing maximum mixing ratios in the BL, which then decrease into the mid-troposphere. This is coupled with a clear enhancement at the altitude of convective outflow (e.g., Pan et al., 2017). Bromoform is a particularly good example as it is commonly examined for signatures of convective influence due to its oceanic emission sources. It is also of particular interest to stratospheric ozone chemistry, as organic halogen species participate in ozone-destroying reactions in the UTLS (Ellis et al., 1996; Pickering et al., 1990; Quack & Wallace, 2003).

Species with “long” lifetimes, defined here as >1 year, exhibit a typically homogenous vertical distribution throughout the troposphere, reflecting their lifetimes to be longer than the time scale of troposphere turnover (Prather et al., 2011). This is seen in dichloromethane and carbon tetrachloride (Figure 2) as well as CFC-11 (Figure 3).

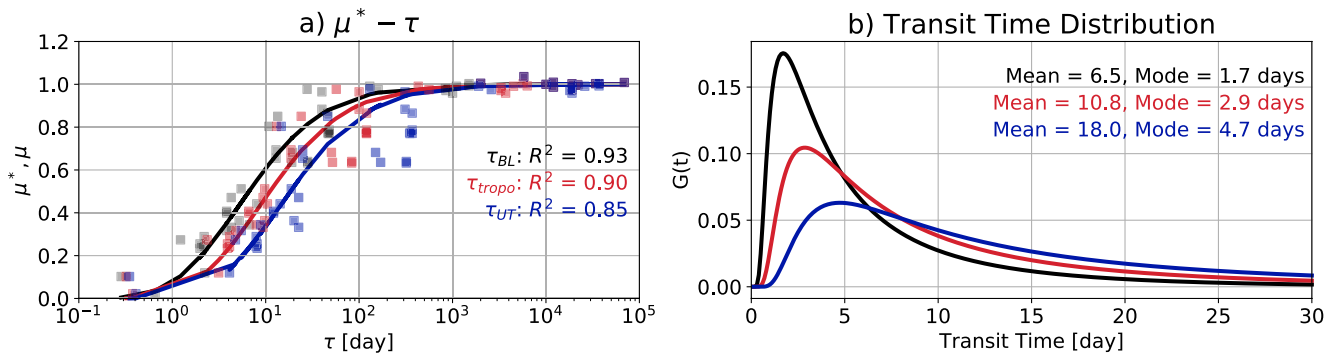


Figure 4. (a) Observation-based μ^* and derived μ - τ curves for the three sets of lifetime conditions: τ_{BL} (black), τ_{TROPO} (red), and τ_{UT} (blue). (b) The resulting transit time distributions for each set of lifetime conditions, $G(t)$, with corresponding modal and mean transit times. Although $G(t)$ is shown for the 0–30 days range, the regression is performed for the range of panel (a) up to 69,000 days, which corresponds to the longest lifetime trace gas used, CFC-114. The integral of $G(t)$ over the entire range is verified to be 1.

6. Characterizing Uncertainties Due to Constant Lifetimes and BL Approximations

6.1. Uncertainty Related to the Approximation of VOC Lifetimes

As shown in Section 4, the VOC lifetimes often have a large range of variation from lower to upper troposphere. It is necessary to characterize the range of uncertainty in the derived TTD from using a constant lifetime approximation in Equation 2. Here we examine the response of the μ - τ relationship and resulting $G(t)$ using the three sets of lifetimes described in Section 4, τ_{BL} , τ_{TROPO} , and τ_{UT} , each representing the conditions of BL, tropospheric average, and UT, respectively. The observed UT fractions, μ^* , are used to constrain the solution for all scenarios. The campaign average μ^* is constructed using the average of samples from 12 to 14 km (UT layer) divided by the average of samples from 0 to 2 km (BL layer). As described in Section 3, samples from RF06 and those collected immediately surrounding Guam are excluded.

Figure 4a shows the μ - τ relationship computed using τ_{BL} , τ_{TROPO} , and τ_{UT} . The fit of μ - τ to observed μ^* - τ is strongest for τ_{BL} , with a coefficient of determination (r^2) of 0.93, closely followed by the τ_{TROPO} with an r^2 of 0.90. Both the τ_{BL} and τ_{TROPO} curves exhibit a tight fit with few outlying points. The μ - τ curve for τ_{UT} has a slightly poorer fit with r^2 of 0.85. There is an increased offset between the modeled curve and the observed UT fractions μ^* , for species with τ_{UT} in the range of 100–350 days, such as chloroform, ethane, and dibromomethane.

The corresponding $G(t)$ in Figure 4b shows a shift to longer mean and modal transit times for results calculated using τ_{TROPO} and τ_{UT} compared to the τ_{BL} , consistent with the increasing lifetimes under the tropospheric average and UT conditions. This shift resulted in an approximate factor of two increase of modal/mean transit times for the tropospheric average conditions, and a factor of 3 for the UT conditions. An independent estimate of transit time using convective mass flux gives a mean transit time of 6–19 days, broadly consistent with the range of uncertainty associated with trace gas lifetimes (Masunaga & Luo, 2016). Sensitivity to calculated lifetime value is greatest for species with lifetimes less than ~ 100 days, and changes to the very long lifetime species has little to no effect on the TTD result.

Using these three sets of lifetimes, τ_{BL} , τ_{UT} , and τ_{TROPO} , Figure 4 indicates the range of uncertainty of TTD in the observed UT related to this approximation. Physically, the appropriate constant lifetime depends on the transport pathways. For the remaining analyses in this study, however, we will use the result of troposphere average lifetimes, and consider that to best represent the layer of interest.

6.2. Uncertainty Related to the Approximation of BL Source Representation

In this study, campaign average measurements in a 2-km layer asl are used to represent the BL mixing ratios, which are then used to compute the UT fractions. In this section, we discuss the uncertainty intro-

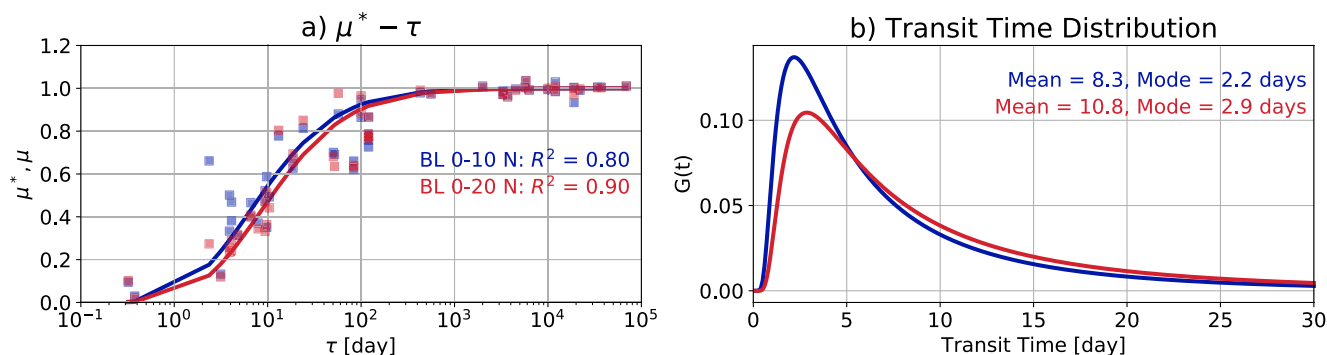


Figure 5. (a) Observation based μ^* and derived μ - τ curves for two boundary layer (BL) representations. Calculations using BL samples from 0° to 20°N (entire study extent) are shown in red, and those using BL samples from 0° to 10°N (the highly convective deep tropics) are shown in blue. (b) Derived transit time distributions for the two BL conditions with corresponding mean and modal transit times.

duced by this approximation. Although in general, the mixing ratios of the selected species are expected to have spatial and temporal variability over the campaign domain and time period, we expect the campaign average provides a reasonable representation for the regional source of transport (Donets et al., 2018; Quack & Wallace, 2003). A potentially larger issue is that the sampled UT layer may have source contributions outside the experimental domain that the CONTRAST data do not represent.

This uncertainty is investigated with the support of trajectory analysis in the companion paper WPS21. In this companion work, kinematic trajectory model TRAJ3D (Bowman, 1993; Bowman & Carrie, 2002) is used to calculate trajectories originating from the same set of airborne measurement points discussed herein, calculated for 60 days back in time from the sampling time. The distributions of the time it takes trajectories to go from the sampling point to the top of the BL for various cases are analyzed as TTDs. Among the four (re)analyses wind products explored for the calculation, the ERA5 reanalysis (Hersbach et al., 2020) produced the best result when evaluated using the chemical observation-based TTDs from this work. The trajectories calculated using ERA5 will be used in this section to assist in the discussion of uncertainties from representing transport sources using the CONTRAST campaign average in the BL.

Using the trajectory analysis, two types of source distribution maps are produced: the distribution of the convection and the BL sources for the UT measurements (see Figures 3 and 4 in WPS21). The analysis using the ERA5 driven trajectories show that nearly 96% of the measurements of interest are influenced by TWP regional convection. The back-trajectories encounter convection mostly in the latitude band 0° - 10°N , with significant additional convective contributions from the warm pool region in 0° - 10°S . Similarly, the distribution of the BL sources is also concentrated in 10°S - 10°N .

To understand the likely impact from the low latitudes and south of the Equator, we examined the surface distribution in the study domain of two leading oceanic species, bromoform and dibromomethane, from a model run using the Community Atmosphere Model with Chemistry (CAM-chem), a component of the NCAR Community Earth System Model (CESM) (Lamarque et al., 2012; Wang, Hornbrook, et al., 2019, Wang, Kinnison, et al., 2019). The result is given as Figure S1. The surface distribution of these two trace gases provides an example of latitudinal gradient of surface mixing ratios correlating with high sea surface temperatures, stronger convection, and associated vertical motions at lower latitudes (south of 10°N). Furthermore, it is known that other chemical species included in this study have cross-equatorial gradients. The combination of a latitudinal gradient in BL trace gas mixing ratios and a strong southerly source for trajectories suggests that the BL trace gas composition closer to the Equator may be more representative source region than the BL of the entire domain (0° - 20°N). However, our measurements are limited to the region north of the Equator. Fully exploring contributions from south of the Equator will require the use of model analysis in future studies.

Based on these considerations and the trajectory model results, we designed a sensitivity test on how the TTD responds to using the BL observations from the entire study area, 0° - 20°N , versus only the highly con-

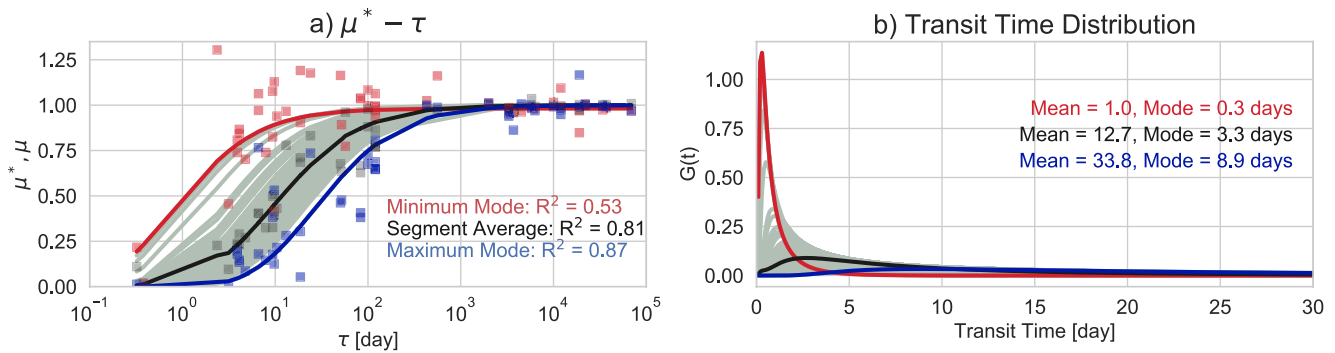


Figure 6. (a) Observation based μ^* and derived μ - τ curves for 148 segments of UT air mass in the 12–14 km UT layer are shown (gray). Curves corresponding to the shortest (red) and longest (blue) transit times are highlighted, and their observed μ^* scatter is shown. The curves for the average of all segments are shown in black, and each individual air mass with r^2 greater than 0.5 are shown in gray. (b) The derived transit time distributions, $G(t)$, and corresponding mean and modal transit times are shown for the shortest (red) and longest (blue) transit time segments, and the average (black).

vective deep tropics, 0° – 10° N. The campaign-average UT mixing ratios are used in both cases. The results are shown in Figure 5, where Figure 5a shows the μ - τ relationship for the entire study area (red) versus the deep tropics (blue), and Figure 5b shows the TTDs with the modal and mean transit times. Note that the red curves in Figures 4 and 5 are identical. Overall, the results show a \sim 20–25% change in mode and mean transit times toward shorter time. This sensitivity test suggests that the approximation of using campaign domain average likely produce smaller uncertainty on the derived TTD than those caused by lifetime uncertainty in Figure 4.

7. Information Content in the Measurements for Representing Atmospheric Variability

Up to this point, we have focused on the TTDs derived using campaign averages. The resulting μ - τ relationship and TTDs represent a regional characterization of the TWP. In this section, we investigate whether the measurements from smaller segments provide sufficient constraint for deriving TTDs for local conditions. The distribution of transit times derived from these individual flight segments, if they contain sufficient information, should show variability in the transport time of these targeted air masses. The analysis of selected periods during the campaign should also inform us on how effectively the method can capture dynamical variability in the campaign domain. The comparison of the campaign average results to TTDs based on individual sample segments will also illuminate physical consistency of the method.

We explore the information content of smaller sample subsets in two steps. First, we identify suitable sample segments and analyze the range of variation in the resulting mode/mean of TTDs from these segments. Comparisons of the “ensemble” mean of the mode/mean with the campaign average result provide a consistency check on the approximations. Second, we examine the transport pathways of two selected sample air masses that represent short and long transport pathways as indicated by the mode/mean of their TTDs using the support of trajectory modeling (see WPS21).

Note that the term “information content” is often used in satellite retrievals to quantify the degree of freedom the inversion can resolve based on the modeled instrument sensitivity. Similarly, we use this term to capture the concept of exploring the sensitivity of these airborne measurements in resolving the dynamical variability sampled by the campaign. Mathematically, the process of solving the Green’s function using the inverse Laplace transform constrained by these measurements is a retrieval problem.

7.1. Variability Represented by UT Segments

To examine the range of variability in the TTDs from segments, we first identify suitable locally averaged UT samples for constraining the regression to derive the TTDs as described in Equations 1–3 (Section 2). These segment-averages are chosen to include one individual AWAS sample and the co-located TOGA measurements within a 3-min window from the start and end of each AWAS collection time, which to-

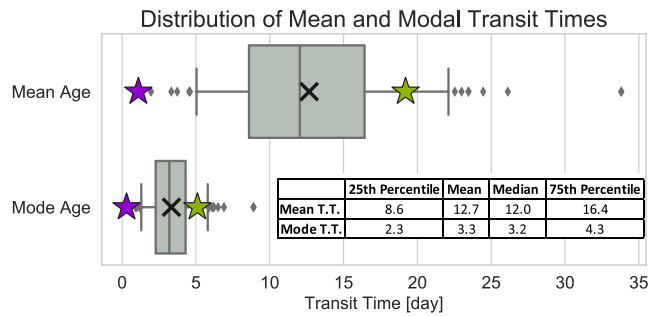


Figure 7. Distributions of modes and means of the 148 segments of UT air masses as shown in Figure 6. Boxes show the interquartile range, while whiskers correspond to the 5th and 95th percentile of the data. Outliers are shown by diamonds. Stars show the position of modes and means for the short (purple) and long (green) transit time cases discussed in Section 7.2. Values for first and third quartile, mean, and median values for mode and mean transit time data are printed on the figure in unit “day.”

the extremes, around the average mode of 3.3 days. Means vary from 1.0 to 33.8 days, around the average mean of 12.7 days.

The UT sample corresponding to the longest modal transit time (blue, $r^2 = 0.86$) shows a compact fit and markedly lower μ^* values for the short and intermediate lifetime species (in the range of lifetimes up to a year) as compared to the ensemble average (black). This is in contrast to the shortest mode segment (red, $r^2 = 0.58$) which shows a μ^* with a large scatter, and some $\mu^* > 1$. It is typical for the μ - τ relationship for an individual air mass to be less compact compared to the UT fractions derived from the campaign average. The μ^* in the range of up to 100 days of lifetimes show most variation from segment to segment. The large variability in μ^* for species with lifetimes between 1 and ~ 100 days reflects the fact that their vertical distributions are strongly dependent on variations in the convective influence for the individual cases (see Section 5, Figures 2 and 3). UT fraction variability is minimal for species with lifetimes of 100 days or greater as a result of their relatively homogenous mixing ratios throughout the troposphere. Because of their sensitivities to convection, the information of convective transport is largely contained in the UT concentrations of these short to intermediate lifetime species. For the shortest modal transit time curves, the μ^* fractions approach (and occasionally exceed) 1 for many species with short and intermediate lifetimes, indicating comparable mixing ratios in the sampled UT and the regional BL. Conversely, the longest transit time cases show depressed μ^* values, consistent with aged air masses.

Figure 7 shows the distribution of the 148 TTD mode and means calculated from the locally averaged UT samples. Average mean and modal transit times computed from all air masses (12.7 and 3.3 days) are comparable to but longer than the campaign average (10.8 and 2.9 days). The median transit times of all air masses (12.0 and 3.2 days) has a slightly closer agreement with the campaign average. The overall consistency between the campaign average derived TTDs and the mean from the local-averaged samples supports that there is sufficient information in these samples for deriving TTDs, which represents dynamical variability and demonstrates the robustness of the method. This ability to construct meaningful locally averaged TTD significantly extends the application of the metric to examining the transport in the wide range of conditions throughout the study area. This point deserves further investigation, which is the focus of the next section.

7.2. Information in the Locally Averaged TTDs in Representing Variable Dynamical Conditions

To further explore the information content of the TTDs from locally averaged samples, we constructed two sampling clusters where one represents the shortest mode/mean of transit time, and the other represents a relatively long mode/mean. Clusters are created using three adjacent AWAS samples showing similar trans-

tals approximately ~ 6.7 min of sampling (Donets et al., 2018) and represents air masses of approximately 94-km in horizontal dimension. As a result, we have a total of 154 UT local-average samples, and each is used to constrain a TTD ($G[t]$) using the same regression procedure. The campaign-average (0° – 20° N) BL mixing ratio is used as the source of the transport to compute the UT fractions, μ^* , for each air mass. The tropospheric average lifetimes, τ_{TROPO} , are used in the calculations.

Figure 6a shows the μ - τ relationship for each of the UT air masses (gray). The observed μ^* scatter for each is omitted for visual clarity, but is shown for two extreme samples with the shortest (red) and longest (blue) modal transit times. The ensemble average of all samples (black) falls in between the two extremes, with the mode and mean similar to the result from the campaign average (Figure 4). We set a criterion to disqualify the samples with r^2 value lower than 0.5 in the μ - τ fit. As a result, 148 out of 154 individual samples are included in this analysis.

The TTDs produced for each sample are shown in Figure 6b. The curves associated with the longest (blue) and shortest (red) transit times are highlighted. The modal transit times vary from 0.3 days up to 8.9 days for

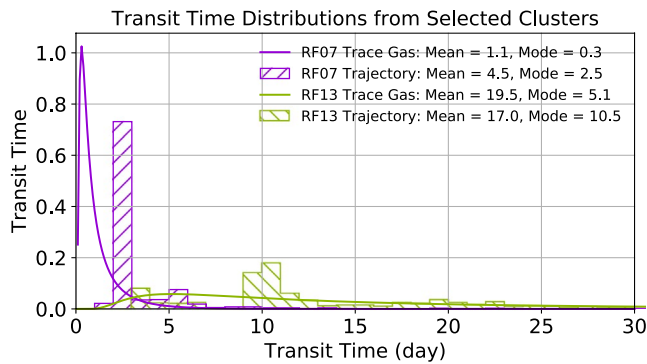


Figure 8. Transit time distributions for the RF07 (purple) and RF13 (green) case study air masses calculated using the chemical lifetime-based approach (solid line) and determined using back-trajectories (histograms).

port behaviors and co-located TOGA measurements. The larger group of samples improve data precision and reduce noise.

The shortest TTD case is from RF07, which took place on 29 January 2014. Consecutive segments collected at 00:38:42, 00:49:20, and 00:53:09 UTC are averaged to produce a μ - τ fit that yields an r^2 of 0.66. The long TTD case is from RF13, which took place on 19 February 2014. Samples collected at 18:42:47, 18:48:47, and 18:54:47 UTC are averaged to produce this air mass with a quite compact μ - τ relationship with an r^2 of 0.89. Although the RF13 cluster does not represent the longest mode and mean transit times from the campaign, its mode/mean are within the fourth quartile (see Figure 7) and represents a scenario for a relatively long transit time sample. The μ^* scatter and μ - τ curve are not shown for these two cases but are similar to the red (short mode, RF07 case) and blue (long mode, RF13 case) examples in Figure 6a. The modes and means from the cases' resulting TTD are shown by purple (RF07) and green (RF13) stars in Figure 7. The derived TTDs for the cases are shown in Figure 8. The RF07 case has mode and mean values of 0.3 and 1.1 days, and the RF13

case has mode and mean values of 5.1 and 19.5 days, respectively.

The dynamic background and transport pathways for these two selected air masses are demonstrated in Figures 9 and 10. Figure 9 shows the flight tracks and wind speeds measured onboard the GV, overlaid with MTSAT-2 thermal IR cloud top temperatures for the nearest time of the two samples. Also shown is the 200 hPa wind field from the ERA5 reanalysis (Hersbach et al., 2020) for the available time closest to the measurements. The key information provided in Figure 9a is that the RF07 case is downwind of a large, active deep convection system south of the Equator, east of the Solomon Islands. This direct convective influence contributed to the short mode/mean transit times for the sampled air mass. From a broader perspective, this convective system is part of the climatological pattern of the Intertropical Convergence Zone (ITCZ) and South Pacific Convergence Zone (SPCZ), (e.g., Waliser & Gautier, 1993). An animation of the dynamical background for 24 h starting 12 h before RF07 is also provided as a Supporting Information (Movie S2).

In contrast to RF07, RF13 were designed to study photochemical evolution in the dynamically stagnated UT. The flight plan was made to repeatedly sample the stagnation point in the center of a persistent anticyclone (Pan et al., 2017). The dynamical background presented in Figure 9b shows that the identified segment of sampling is located near the zero-wind point at the center of the large-scale UT anticyclone. It is noteworthy that this point is somewhat offset from the center of the “bowtie” flight pattern, near 12°N and 160°E, designated to be the repeated sampling point based on the forecast. Additionally, while there is active convection south of the flight track, the UT flow pattern as indicated by the 200 hPa wind hindered immediate convective influence to the flight segment. The TTD identified as having a long mode/mean transit time is consistent with this dynamic setting.

To further verify the information represented by the two samples, the transport pathways and transit times are investigated using trajectory model analysis. Details of the trajectory model and calculations are described in the companion paper WPS21 and briefly introduced in Section 6.2. A cluster of 75 backward trajectories are initiated at each of the three samples from both RF07 and RF13, for a total of 225 trajectories launched for each case. Trajectories are traced backward from the point of sampling until their reaching the top of the BL, thus giving a “transit time” from the BL to the sampling point. The results of this analysis are shown in Figures 8 and 10.

In Figure 8, TTDs for the two air masses produced using the clusters of trajectories are compared with that of the chemistry-based approach as described in Section 7.1. Although the trajectory-based TTDs are consistently offset to longer mode/means compared to the chemical-lifetime based TTDs, they clearly show the sharp contrast of the transport histories between the two cases. This result supports the transport information content in chemical lifetime-based TTDs derived from local-segment averages. The offset between the two sets of TTDs reflects the limitation of the kinematic trajectory models in representing convective

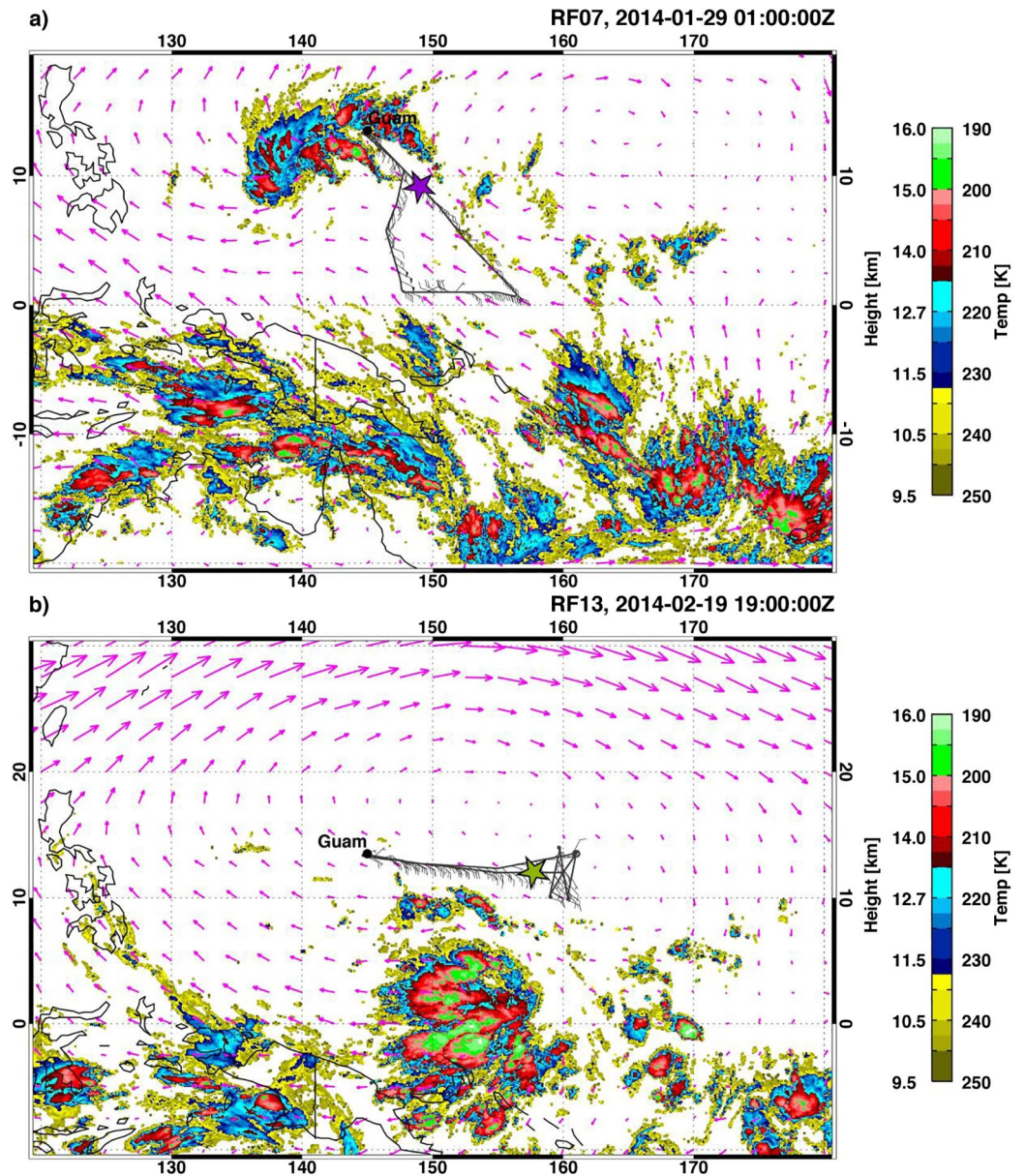


Figure 9. The dynamical background for (a) the short transit time case (RF07) at 01:00:00 Z on January 29, and (b) the long transit time case (RF13) at 19:00:00 Z on February 19, 2014. The flight tracks are shown in black with wind barbs representing the wind measurements onboard the Gulfstream V. The location of the short transit time sample cluster is marked by the purple star and the location of the long transit time case is marked by the green star. The yellow-green shading shows the cloud top temperature from the MTSAT-2 Thermal IR channel indicating the locations of active convection and outflows. The estimated cloud top height in km is labeled on the color-scale. The pink arrows show the 200 hPa winds from ERA5, which correspond approximately to the Gulfstream V's flight level in the UT.

transport using resolved winds. The grid size of the reanalysis wind does not permit the representation of small-scale rapid updraft, the result of which contribute to the vertical mixing and the enhanced short-lived VOC's at the UT.

Figure 10 shows the back-trajectories for the two air masses as “spaghetti plots.” The trajectory tracks are shown to linger and spread at different altitudes as indicated by the track color, and the trajectories BL termination points are colored by their transit time (trajectory length in time between the sampling point and the top of the BL). The stark contrast between the trajectory behavior in the two cases provides support

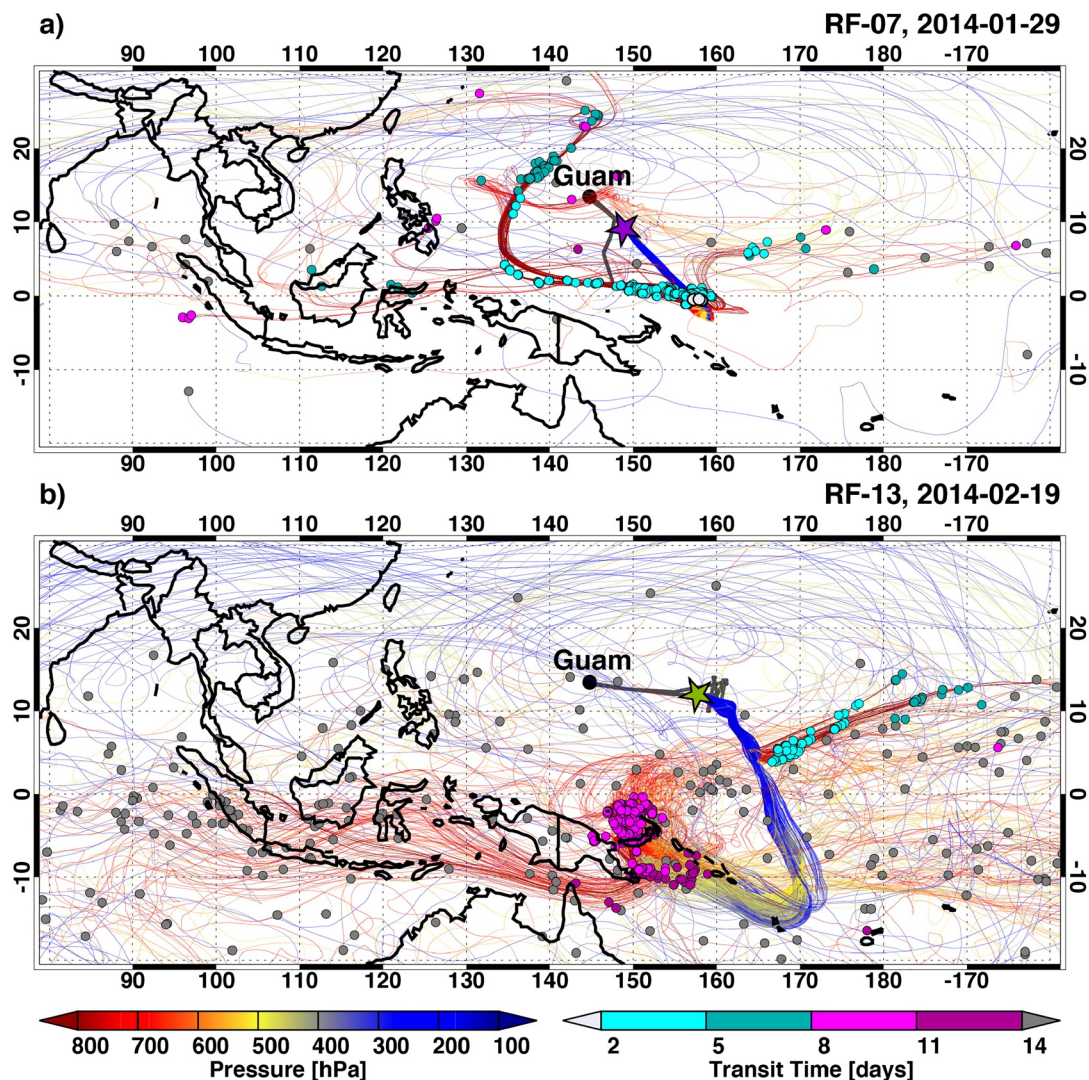


Figure 10. “Spaghetti plots” of backward trajectories launched from the locations of the two measurement clusters of interest. The RF07 case (marked by the purple star) is shown in panel (a) and the RF13 case (green star) is in panel (b). Back trajectory tracks are colored by their pressure, and terminate upon reaching the top of the boundary layer, at which time they are marked with a dot colored according to the transit time.

from dynamical information for the chemical-observation based approach. A large fraction of the air parcels in the RF07 air mass experienced rapid vertical transport near the Equator and 150°–160°E, the region east of the Solomon Islands. These parcel trajectories terminate in the BL within 2–5 days. The majority of the back trajectories reached the BL within a week, consistent with the short mode/mean transit times for this air mass (Figure 8). In contrast, the distribution in the RF13 case is highlighted by the lingering of back trajectories in the UT before terminating in the BL within 8–14 days. A small fraction of trajectories show influence from convective transport near 5°N and 162°E, roughly 5 days before the case’s observation. A larger convective event can be identified around 10 days before sampling. A large fraction of air parcels have transit times longer than 2 weeks, consistent with the long mode and mean transit times calculated for this case (Figure 8).

These two cases from RF07 and RF13 highlight the wealth of information in the segment averages, which enables the method to identify a wide range of transport conditions using the composition of the air masses sampled throughout the study area. The rich information contained within each sample expands the application of these chemical observation-based TTDs as a metric to bridge chemical observations and diagnos-

ing transport. Trajectory results presented in the companion paper provide useful information regarding the potential BL sources contributing to the sampled TWP UT.

Note that the data from individual samples is expected to have larger measurement uncertainties compared to the campaign average. This is reflected in the distribution of r^2 of the fit and the large scatter of segment-averaged μ^* relative to the derived $\mu\text{-}\tau$. The r^2 for individual samples included in this study ranges from 0.53 to 0.95, with a mean r^2 of 0.81 ± 0.09 . This is $\sim 10\%$ lower than the campaign average data r^2 of 0.90. While we expect the mode/mean values of these TTDs from individual measurements to be inherently less certain, the two case-analyses indicate that they provide physically meaningful representations of dynamical variability in the regional transport.

8. Conclusions and Discussions

The analysis presented in this work aims to quantitatively characterize the approximations made in deriving TTD as a transport metric using *in-situ* VOC data, as well as their impact on the calculated transit times. These characterizations are essential for understanding the limitations of the chemical-observation based TTD and the application of these results for model diagnostics. Our analysis focuses on (a) understanding the range of variability in VOC lifetimes and the resultant implications of the required approximations, (b) sensitivities and limitations of using campaign-averaged BL measurements to represent transport origins for the UT measurements, and (c) the information content in the data in relation to the representation of dynamical variability in the transport conditions sampled by the campaign. The key results and conclusions are summarized below.

First, the approximation made for the VOC lifetimes was identified as the largest source of uncertainty of this method. The estimated chemical lifetimes increase from BL to UT by a factor of 2–10 among most short to intermediate lifetime species, which are the ones primarily responsible for the changes in the derived TTD. The corresponding TTD mode and mean vary by approximately a factor of 3, with means ranging from 6.5 to 18 days. Despite the uncertainty, the resulting mean transit times are consistent with the transit time inferred from a convective mass flux-based estimate of 6–19 days (Masunaga & Luo, 2016). With this quantification of variability, we consider the troposphere average lifetime to be the preferred approximation for the layer of interest in this study. A better approximation for the layer-averaged lifetimes may be explored in follow up studies involving chemistry models.

Second, the approximation of using the campaign average BL measurements to represent the source of transport for the UT measurements is found to be a smaller source of uncertainty for the derived TTDs. However, this uncertainty may need further assessment. The BL measurements we have from the campaign are limited to the NH, while our RF07 case study (Section 7.2) and a companion trajectory model study (WPS21) both indicate that the contribution from the region of active convection associated with ITCZ and SPCZ south of the Equator are making important contributions. This issue will be further investigated in follow up studies with the help of global models.

Lastly, the TTD analysis is applied to 148 flight segments with each representing an air mass of the spatial scale of ~ 94 km. The physical consistency of these individual sample derived transit times is verified against the domain average transit times. The results show that the averages of the modes and means from individual air masses are consistent with the mode and mean derived using campaign-average data. This consistency adds additional support to the robustness of the method and also significantly broadens the application of this diagnostic. Specifically, the application of the metric is now possible for a range of TWP conditions. The physical information in the segment-averaged samples is further demonstrated using 2 extreme cases with the support of the trajectory analysis (Section 7.2, and WPS21).

Overall, these quantitative analyses significantly improve our understanding of the strengths and limitations of the airborne observation-based TTD as demonstrated in Luo et al. (2018). While the approximations of chemical lifetimes and assuming the local BL as the source of transport for the VOC observed in the UT concentrations are inspired and supported by the compact $\mu^*\text{-}\tau$ relationship which led to the development

of the approach, they are also intrinsic sources of limitations for the method. In this particular analysis, the conditions of intense TWP convective transport dominates the vertical redistribution of trace gases between the BL and the layer of the main outflow in the UT. It is unclear how the approximations would be successful for regions of different dynamical background. For example, the application of the method for a layer above the main convective outflow may show much larger uncertainties, since the sources contributing to the tropopause region measurements are likely more complex, and they potentially include much broader regions of BL and layers above the measurement-level, such as the lower stratosphere. The non-unique source region will challenge the quasi-one-dimensional approximation as well as further complicating the approximation of lifetimes. These are future research issues that will be addressed using high altitude observations and chemistry climate models.

The relationship between trace gas lifetimes and their atmospheric distributions and variability as a tool for understanding atmospheric behaviors has a long history (e.g., Jobson et al., 1999; Junge, 1974). Exploring this relationship and how it can be used to quantify transport timescales in a convection-dominated tropospheric region is a new direction of progress achieved in this work. We expect this diagnostic to bridge airborne observations and various models in understanding and improving the representation of convective transport. The first application of this kind has been performed to evaluate the representations of convective transport by kinematic trajectory models and the performance of four major analysis and reanalysis wind products (WPS21). Follow-up studies using global chemistry climate models are expected to further expand the understanding of the method.

Appendix A: Lifetime Calculations

The oxidant OH rapidly reacts with most trace gas species, is considered the most active and ubiquitous chemical scavenger, and is the most important oxidizing agent in the atmosphere. Reaction with OH is the primary control on species' atmospheric lifetime and mixing ratio as a result of its ability to react with and thereby destroy the bulk of chemical species it encounters (Holland et al., 2003; Jobson et al., 1999; Nicely et al., 2016; Tan et al., 2001). Local OH lifetime of a trace gas can be estimated using Equation A1, where (OH) is OH number density measured in molecules cm^{-3} , and k is the temperature dependent rate constant of reaction (Levine, 2003; Kurylo & Orkin, 2003).

$$\tau_{OH} = \frac{1}{k(T) * [OH]}, \quad (A1)$$

Temperature dependent rate constants are unique for each species and are determined experimentally and reported in literature. Values utilized here are compiled primarily from the International Union of Pure and Applied Chemistry (IUPAC, 2020) recommended values and the National Institute of Standards and Technology (NIST) database (<http://iupac.pole-ether.fr/index.html>; <https://kinetics.nist.gov/>). Others were collected from Atkinson and Aschmann (1989), Atkinson (2003), and Calvert et al. (2011). Temperatures in the UT, BL, and troposphere average are calculated from CONTRAST measurements and are found to be 215.8, 296.6, and 256.2 K, respectively. A 24-h average observationally constrained (OH) estimate for January–February is obtained from Nicely et al. (2016) where CONTRAST campaign measurements of chemical species, radiative variables, and meteorological parameters are utilized to estimate *in-situ* production and loss of OH. To calculate τ_{OH} for the UT, BL, and troposphere average (OH) estimates used are 1.0×10^6 , 2.5×10^6 , and 1.6×10^6 molecules cm^{-3} , respectively.

It is noted that for some species rate constants are extrapolated for temperatures outside the recommended range. For example, benzene (recommended range is 230–350 K) and chlorobenzene (recommended range 234–296 K) are extrapolated to 216 K for UT conditions. DMS is similarly extrapolated (recommended range 240–360 K) in addition to having an O_2 dependence. The O_2 number density is calculated using average pressures in the UT and BL troposphere average of 180 hPa and 940 hPa respectively. Rate constants for butyl nitrate -2 and -n were only available at 298 K, so it is assumed those species have a similar temperature dependence to isopropyl nitrate. Their rate constants at 298 K are scaled accordingly for the tropospheric average and UT temperatures.

Table A1
The Troposphere τ_{OH} , τ_{photo} , and Combined τ_{TOTAL} for VOCs That Have Both OH and Photolysis Loss

Trace gas	Chemical formula	τ_{OH} (day)	τ_{photo} (day)	τ_{TOTAL} (day)
Acetaldehyde	C ₂ H ₄ O	0.4	1.7	0.32
2-Butyl Nitrate	C ₄ H ₉ NO ₃	8.8	10	4.8
n-Butyl Nitrate	C ₄ H ₉ NO ₃	4.6	9.9	3.1
Isopropyl Nitrate	C ₃ H ₇ NO ₃	29	11	7.9
Ethyl Nitrate	C ₂ H ₅ ONO ₂	51	18	13
Bromoform	CHBr ₃	72	25	19

Separately from OH decay, the photolysis decay pathway acts to destroy trace gas molecules by photodissociation caused by incident solar radiation. The rate of this destruction pathway depends on the properties of the trace gas as well as the strength of solar radiation striking the local atmosphere (King, 2013, ECG Environmental Brief No. 1; Tang et al., 2003). This reaction does not occur for all chemical species, and is only applied to the following photochemically active species: acetaldehyde, n-butyl nitrate, 2-butyl nitrate, isopropyl nitrate, ethyl nitrate, and bromoform (Speight, 2017). The troposphere τ_{OH} , τ_{photo} , and combined τ_{TOTAL} for species that consider photolysis loss are shown in Table A1.

The rate loss of a chemical due to photolysis decay is quantified using term J , a first-order reaction decay constant coefficient that depends on the photochemical radiation and photophysical properties of a chemical. J is directly related to photolysis lifetime, τ_{photo} via:

$$\tau_{photo} = \frac{1}{J}. \quad (A2)$$

Estimates of J are obtained by Atmospheric Radiation and Measurements (ARIM) group at National Center for Atmospheric Research (NCAR). The High-performance Instrumented Airborne Platform for Environmental Research (HIAPER) Airborne Radiation Package (HARP) Actinic Flux instrument aboard the CONTRAST GV aircraft measures spectrally resolved upwelling and downwelling actinic flux in the range of 300–640 nm. *In-situ* photolysis rates are calculated along the flight track using a modified version of the NCAR Tropospheric Ultraviolet and Visible (TUV) radiative transfer model.

The TUV model was also used to calculate clear-sky actinic flux and J -values along the flight track. The ratio of measured to clear-sky modeled photolysis frequencies were then calculated in the study domain (130°–165°E, 0°–20°N, restricted to solar zenith angles less than 50°) and binned by altitude to approximate aerosol and cloud impacts on photolysis rates.

These altitude-binned ratios were then applied to a clear-sky 24-h TUV model run and summed to provide a daily integrated J for each molecule. TUV was run on the mid-date of the project (February 4, 2014) at the center of the latitude domain (10°N). The seasonal changes in actinic flux result in a change in total daily

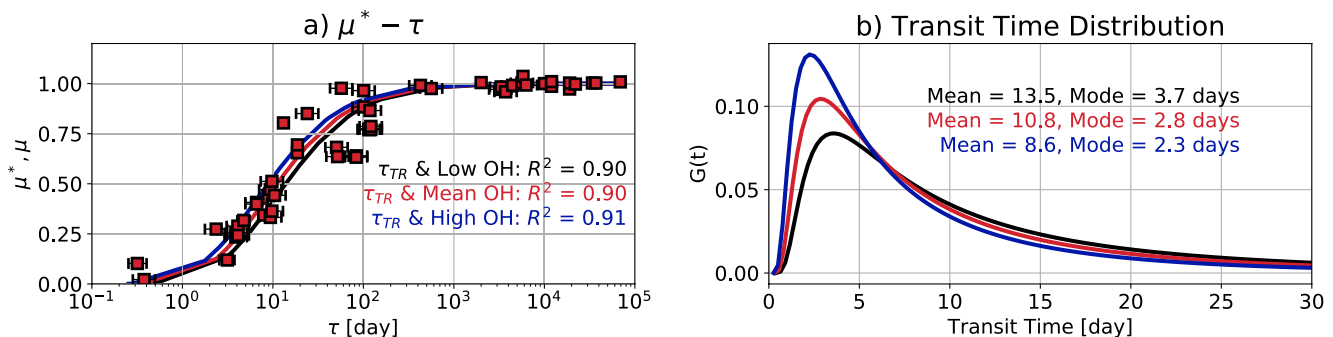


Figure A1. (a) The μ - τ curve for varying lifetime conditions: τ_{total} for the troposphere using mean (red) lower bound (black), and upper bound (blue) OH estimates. The observation based μ^* scatter shown uses lifetime using mean OH as the marker, and whiskers are lifetimes corresponding to upper and lower bound OH estimates. (b) The $G(t)$ relationship with corresponding mean and modal transit times are shown.

values of +6%–8% (molecule dependent) from the beginning to end of the project. The ozone column was set at 246 Dobson units, near the middle of Ozone Monitoring Instrument (OMI) satellite retrievals in the domain. The full OMI range results in $\pm 3\%$ changes in the studied J-values. No aerosols or clouds were included, the measured temperature profile was altitude-binned with the ratios and the albedo was set at 0.06.

Appendix B: Uncertainty Related to OH Estimate

The mean of the 24-h average observationally constrained (OH) estimate from Nicely et al. (2016) is used to calculate lifetime approximations. Those mean values are bounded by variability, which introduces variability to the lifetime estimates. Here, the impact of OH variability on troposphere lifetime is examined. A lower bound of 1.2×10^6 molecules cm^{-3} and upper bound of 2.1×10^6 molecules cm^{-3} is used. The mean value is the same as that used in Section 4, 1.6×10^6 molecules cm^{-3} . It should be noted that a 24-h [OH] estimate may introduce additional uncertainty for the shorter-lived species.

The μ - τ relationship using τ_{TROPO} computed with the three OH estimates is shown in Figure A1. All three lifetime estimates have a very good fit with r^2 values of 0.90–0.91. The variability bounds for the lifetime estimates are shown by horizontal bars on the μ^* scatter. The resulting $G(t)$ are also shown, with means ranging from 8.6 to 10.8–13.5 days and modes ranging from 2.3 to 2.8–3.7 days. Estimates using higher OH values tend to have faster destruction and therefore shorter lifetimes. As demonstrated in this paper, the use shorter lifetime estimates (for the same μ^* scatter) with the tropospheric TTD method typically leads to shorter mode and mean transit times. This adds additional uncertainty to that associated with the use of a constant lifetime approximation.

Conflict of Interest

The authors declare no conflicts of interest relevant to this study.

Data Availability Statement

The CONTRAST experiment was funded by NSF. CONTRAST flight data used in this study are available from the NCAR/UCAR EOL data archive (https://data.eol.ucar.edu/master_lists/generated/contrast/) and the field catalog provides all mission information (<http://catalog.eol.ucar.edu/contrast>). ERA5 reanalysis data can be accessed from the NCAR/UCAR research data archive (<https://rda.ucar.edu/datasets/ds633.0/>).

Acknowledgments

This work is part of SC's PhD research, supported by the National Aeronautics and Space Association (NASA) Future Investigators in NASA Earth and Space Science and Technology (FINESST) program under the grant 80NSSC19K1353 awarded to the City University of New York (CUNY). Z. J. Luo acknowledges NASA grants 80NSSC17K0197, 80NSSC20K0089. E. Apel acknowledges support from National Science Foundation (NSF) grants ATM1261689 and ATM1853948 and NASA grant NNX17AE43G. W. P. Smith acknowledges support from NSF grant AGS-1853929. This work is also supported by the National Center for Atmospheric Research (NCAR). NCAR is operated by the University Corporation for Atmospheric Research and sponsored by the NSF.

References

- Albu, M., Barnes, I., Becker, K. H., Patroescu-Klotz, I., Mocanu, R., & Benter, T. (2006). Rate coefficients for the gas-phase reaction of OH radicals with dimethyl sulfide: Temperature and O_2 partial pressure dependence. *Physical Chemistry Chemical Physics*, 8(6), 728–736. <https://doi.org/10.1039/B512536G>
- Anderson, D. C., Nicely, J. M., Wolfe, G. M., Hanisco, T. F., Salawitch, R. J., Canty, T. P., et al. (2017). Formaldehyde in the Tropical Western Pacific: Chemical sources and sinks, convective transport, and representation in CAM-Chem and the CCM1 models. *Journal of Geophysical Research: Atmospheres*, 122(20), 11–201. <https://doi.org/10.1002/2016JD026121>
- Andrews, A. E., Boering, K. A., Daube, B. C., Wofsy, S. C., Hints, E. J., Weinstock, E. M., & Bui, T. P. (1999). Empirical age spectra for the lower tropical stratosphere from in situ observations of CO_2 : Implications for stratospheric transport. *Journal of Geophysical Research*, 104(D21), 26581–26595. <https://doi.org/10.1029/1999JD900150>
- Andrews, A. E., Boering, K. A., Wofsy, S. C., Daube, B. C., Jones, D. B., Alex, S., et al. (2001). Empirical age spectra for the midlatitude lower stratosphere from in situ observations of CO_2 : Quantitative evidence for a subtropical “barrier” to horizontal transport. *Journal of Geophysical Research: Atmospheres*, 106(D10), 10257–10274. <https://doi.org/10.1029/2000JD900703>
- Andrews, S. J., Carpenter, L. J., Apel, E. C., Atlas, E., Donets, V., Hopkins, J. R., et al. (2016). A comparison of very short-lived halocarbon (VSLs) and DMS aircraft measurements in the tropical west Pacific from CAST, ATTREX and CONTRAST. *Atmospheric Measurement Techniques*, 9(10), 5213–5225. <https://doi.org/10.5194/amt-9-5213-2016>
- Apel, E. (2014). *NSF/NCAR GV HIAPER TOGA VOC analyzer data (Version 1.0)* (p. 5065). UCAR/NCAR—Earth Observing Laboratory.
- Apel, E. C., Hornbrook, R. S., Hills, A. J., Blake, N. J., Barth, M. C., Weinheimer, A., et al. (2015). Upper tropospheric ozone production from lightning NO_x-impacted convection: Smoke ingestion case study from the DC3 campaign. *Journal of Geophysical Research: Atmospheres*, 120(6), 2505–2523. <https://doi.org/10.1002/2014JD022121>
- Arakawa, A. (2004). The cumulus parameterization problem: Past, present, and future. *Journal of Climate*, 17(13), 2493–2525. [https://doi.org/10.1175/1520-0442\(2004\)017<2493:RATCPP>2.0.CO;2](https://doi.org/10.1175/1520-0442(2004)017<2493:RATCPP>2.0.CO;2)
- Atkinson, R. (1986). Kinetics and mechanisms of the gas-phase reactions of the hydroxyl radical with organic compounds under atmospheric conditions. *Chemical Review*, 85(1), 69–201. <https://doi.org/10.1021/cr00071a004>

- Atkinson, R. (2003). Kinetics of the gas-phase reactions of OH radicals with alkanes and cycloalkanes. *Atmospheric Chemistry and Physics*, 3(6), 2233–2307. <https://doi.org/10.5194/acp-3-2233-2003>
- Atkinson, R., & Aschmann, S. M. (1989). Rate constants for the reactions of the OH radical with the propyl and butyl nitrates and 1-nitrobutane at 298 ± 2 K. *International Journal of Chemical Kinetics*, 21(12), 1123–1129. <https://doi.org/10.1002/kin.550211205>
- Atlas, E. (2014). *NSF/NCAR GV HAPER airborne instrument solicitation (HAIS) advanced whole air sampler. Version 1.0*. UCAR/NCAR—Earth Observing Laboratory.
- Bergman, J. W., Fierli, F., Jensen, E. J., Honomichl, S., & Pan, L. L. (2013). Boundary layer sources for the Asian anticyclone: Regional contributions to a vertical conduit. *Journal of Geophysical Research: Atmospheres*, 118(6), 2560–2575. <https://doi.org/10.1002/jgrd.50142>
- Boering, K. A., Wofsy, S. C., Daube, B. C., Schneider, H. R., Loewenstein, M., Podolske, J. R., & Conway, T. J. (1996). Stratospheric mean ages and transport rates from observations of carbon dioxide and nitrous oxide. *Science*, 274(5291), 1340–1343. <https://doi.org/10.1126/science.274.5291.1340>
- Bowman, K. P. (1993). Large-scale isentropic mixing properties of the Antarctic polar vortex from analyzed winds. *Journal of Geophysical Research*, 98(D12), 23013–23027. <https://doi.org/10.1029/93JD02599>
- Bowman, K. P., & Carrie, G. D. (2002). The mean-meridional transport circulation of the troposphere in an idealized GCM. *Journal of the Atmospheric Sciences*, 59(9), 1502–1514. [https://doi.org/10.1175/1520-0469\(2002\)059<1502:Tmmtco>2.0.Co;2](https://doi.org/10.1175/1520-0469(2002)059<1502:Tmmtco>2.0.Co;2)
- Calvert, J., MelloukiOrlando, A. J., Pilling, M., & Wallington, T. (2011). *Mechanisms of atmospheric oxidation of the oxygenates*. Oxford University Press.
- Carpenter, L. J., Reimann, S., Burkholder, J. B., Clerbaux, C., Hall, B. D., Hossaini, R., et al. (2014). Ozone-depleting substances (ODSs) and other gases of interest to the Montreal protocol, Chapter 1. In *Scientific assessment of ozone depletion: 2014, Global Ozone Research and Monitoring Project—Report* (Vol. 55, p. 105). World Meteorological Organization.
- Cohen, M. A., & Ryan, P. B. (1989). Observations less than the analytical limit of detection: A new approach. *Journal of the Air Pollution Control Association*, 39(3), 328–329. <https://doi.org/10.1080/08940630.1989.10466534>
- Donets, V., Atlas, E. L., Pan, L. L., Schaffler, S. M., Honomichl, S., Hornbrook, R. S., et al. (2018). Wintertime transport of reactive trace gases from East Asia into the deep tropics. *Journal of Geophysical Research: Atmospheres*, 123(22), 12877–12896. <https://doi.org/10.1029/2017jd028231>
- Dvorkin, A. Y., & Steinberger, E. H. (1999). Modeling the altitude effect on solar UV radiation. *Solar Energy*, 65(3), 181–187. [https://doi.org/10.1016/s0038-092x\(98\)00126-1](https://doi.org/10.1016/s0038-092x(98)00126-1)
- Ehhalt, D. H., Rohrer, F., Blake, D. R., Kinnison, D. E., & Konopka, P. (2007). On the use of nonmethane hydrocarbons for the determination of age spectra in the lower stratosphere. *Journal of Geophysical Research*, 112(D12). <https://doi.org/10.1029/2006JD007686>
- Ellis, W. G., Jr., Thompson, A. M., Kondragunta, S., Pickering, K. E., Stenchikov, G., Dickerson, R. R., & Tao, W. K. (1996). Potential ozone production following convective transport based on future emission scenarios. *Atmospheric Environment*, 30(4), 667–672. [https://doi.org/10.1016/1352-2310\(95\)00318-5](https://doi.org/10.1016/1352-2310(95)00318-5)
- Engel, A., Möbius, T., Bönisch, H., Schmidt, U., Heinz, R., Levin, I., et al. (2009). Age of stratospheric air unchanged within uncertainties over the past 30 years. *Nature Geoscience*, 2, 28–31. <https://doi.org/10.1038/ngeo388>
- Eyring, V., Butchart, N., Waugh, D. W., Akiyoshi, H., Austin, J., Bekki, S., et al. (2006). Assessment of temperature, trace species, and ozone in chemistry-climate model simulations of the recent past. *Journal of Geophysical Research*, 111(D22). <https://doi.org/10.1029/2006jd007327>
- Folkens, I., & Martin, R. V. (2005). The vertical structure of tropical convection and its impact on the budgets of water vapor and ozone. *Journal of the Atmospheric Sciences*, 62(5), 1560–1573. <https://doi.org/10.1175/jas3407.1>
- Haine, T. W. N., & Hall, T. M. (2002). A generalized transport theory: Water-mass composition and age. *Journal of Physical Oceanography*, 32, 1932–1946. [https://doi.org/10.1175/1520-0485\(2002\)032<1932:agtwm>2.0.co;2](https://doi.org/10.1175/1520-0485(2002)032<1932:agtwm>2.0.co;2)
- Hall, T. M., & Plumb, R. A. (1994). Age as a diagnostic of stratospheric transport. *Journal of Geophysical Research*, 99(D1), 1059–1070. <https://doi.org/10.1029/93JD03192>
- Hauack, M., Bönisch, H., Hoor, P., Keber, T., Ploeger, F., Schuck, T. J., & Engel, A. (2020). A convolution of observational and model data to estimate age of air spectra in the northern hemispheric lower stratosphere. *Atmospheric Chemistry and Physics*, 20(14), 8763–8785. <https://doi.org/10.5194/acp-20-8763-2020>
- Hersbach, H., Bell, B., Berrisford, P., Hirahara, S., Horányi, A., Muñoz-Sabater, J., et al. (2020). The ERA5 global reanalysis. *Quarterly Journal of the Royal Meteorological Society*, 146(730), 1999–2049. <https://doi.org/10.1002/qj.3803>
- Holland, F., Hofzumahaus, A., Schäfer, J., Kraus, A., & Patz, H. W. (2003). Measurements of OH and HO₂ radical concentrations and photolysis frequencies during BERLIOZ. *Journal of Geophysical Research: Atmospheres*, 108(D4), PHO2-1–PHO2-23. <https://doi.org/10.1029/2001JD001393>
- Holzer, M., & Hall, T. M. (2000). Transit-time and tracer-age distributions in geophysical flows. *Journal of the Atmospheric Sciences*, 57(21), 3539–3558. [https://doi.org/10.1175/1520-0469\(2000\)057<3539:TTATAD>2.0.CO;2](https://doi.org/10.1175/1520-0469(2000)057<3539:TTATAD>2.0.CO;2)
- Holzer, M., & Waugh, D. W. (2015). Interhemispheric transit time distributions and path-dependent lifetimes constrained by measurements of SF₆ CFCs, and CFC replacements. *Geophysical Research Letters*, 42(11), 4581–4589. <https://doi.org/10.1002/2015GL064172>
- Honomichl, S. B., & Pan, L. L. (2020). Transport from the Asian Summer Monsoon Anticyclone over the western Pacific. *Journal of Geophysical Research: Atmospheres*, 125(13). <https://doi.org/10.1029/2019JD032094>
- Hynes, A. J., Wine, P. H., & Semmes, D. H. (1986). Kinetics and mechanism of hydroxyl reactions with organic sulfides. *The Journal of Physical Chemistry*, 90(17), 4148–4156. <https://doi.org/10.1021/j100408a062>
- International Union of Pure and Applied Chemistry. (2020). *Task group on atmospheric chemical kinetic data evaluation search page*. Retrieved from <http://iupac.pole-ether.fr/>
- Jobson, B. T., McKeen, S. A., Parrish, D. D., Fehsenfeld, F. C., Blake, D. R., Goldstein, A. H., et al. (1999). Trace gas mixing ratio variability versus lifetime in the troposphere and stratosphere: Observations. *Journal of Geophysical Research*, 104(D13), 16091–16113. <https://doi.org/10.1029/1999JD900126>
- Johnson, J. E. (1981). The lifetime of carbonyl sulfide in the troposphere. *Geophysical Research Letters*, 8(8), 938–940. <https://doi.org/10.1029/gl008i008p00938>
- Junge, C. E. (1974). Residence time and variability of tropospheric trace gases. *Tellus*, 26(4), 477–488. <https://doi.org/10.3402/tellusa.v26i4.9853>
- King, M. (2013). *Calculating photolysis rates and estimating photolysis lifetimes*. Royal Society of Chemistry, Environmental Briefs, Environmental Chemistry Group Environmental Briefs. Retrieved from <https://www.envchemgroup.com/eb1-calculating-photolysis-rates-and-estimating-photolysis-lifetimes.html>

- Ko, M., Newman, P., Reimann, S., & Strahan, S. (2013). *SPARC report on the lifetimes of stratospheric ozone-depleting substances, their replacements, and related species*.
- Kurylo, M. J., & Orkin, V. L. (2003). Determination of atmospheric lifetimes via the measurement of OH radical kinetics. *Chemical Reviews*, *103*(12), 5049–5076. <https://doi.org/10.1021/cr020524c>
- Lamarque, J.-F., Emmons, L. K., Hess, P. G., Kinnison, D. E., Tilmes, S., Vitt, F., et al. (2012). CAM-chem: Description and evaluation of interactive atmospheric chemistry in the Community Earth System Model. *Geoscientific Model Development*, *5*(2), 369–411. <https://doi.org/10.5194/gmd-5-369-2012>
- Levine, J. S. (2003). *Treatise on geochemistry*. Elsevier Science.
- Li, F., Waugh, D. W., Douglass, A. R., Newman, P. A., Pawson, S., Stolarski, R. S., et al. (2012). Seasonal variations of stratospheric age spectra in the Goddard Earth Observing System Chemistry Climate Model (GEOSCCM). *Journal of Geophysical Research*, *117*(D5). <https://doi.org/10.1029/2011JD016877>
- Liang, Q., Newman, P. A., & Reimann, S. (2016). *SPARC report on the mystery of carbon tetrachloride*.
- Lu, K. D., Rohrer, F., Holland, F., Fuchs, H., Bohn, B., Brauers, T., et al. (2012). Observation and modeling of OH and HO₂ concentrations in the Pearl River Delta 2006: A missing OH source in a VOC rich atmosphere. *Atmospheric Chemistry and Physics*, *12*(3), 1541–1569. <https://doi.org/10.5194/acp-12-1541-2012>
- Luo, Z. J., Pan, L. L., Atlas, E. L., Chelpon, S. M., Honomichl, S. B., Apel, E. C., et al. (2018). Use of airborne in situ VOC measurements to estimate transit time spectrum: An observation-based diagnostic of convective transport. *Geophysical Research Letters*, *45*(23), 13150–13157. <https://doi.org/10.1029/2018GL080424>
- Madronich, S. (1987). Photodissociation in the atmosphere 1. Actinic flux and the effects of ground reflections and clouds. *Journal of Geophysical Research*, *92*(D8), 9740–9752. <https://doi.org/10.1029/JD092iD08p09740>
- Masunaga, H., & Luo, Z. J. (2016). Convective and large-scale mass flux profiles over tropical oceans determined from synergistic analysis of a suite of satellite observations. *Journal of Geophysical Research: Atmospheres*, *121*(13), 7958–7974. <https://doi.org/10.1002/2016JD024753>
- Nicely, J. M., Anderson, D. C., Canty, T. P., Salawitch, R. J., Wolfe, G. M., Apel, E. C., et al. (2016). An observationally constrained evaluation of the oxidative capacity in the tropical western Pacific troposphere. *Journal of Geophysical Research: Atmospheres*, *121*(12), 7461–7488. <https://doi.org/10.1002/2016JD025067>
- Orbe, C., Holzer, M., Polvani, L. M., & Waugh, D. (2013). Air-mass origin as a diagnostic of tropospheric transport. *Journal of Geophysical Research: Atmospheres*, *118*(3), 1459–1470. <https://doi.org/10.1002/jgrd.50133>
- Orbe, C., Waugh, D. W., Newman, P. A., & Steenrod, S. (2016). The transit-time distribution from the Northern Hemisphere midlatitude surface. *Journal of the Atmospheric Sciences*, *73*(10), 3785–3802. <https://doi.org/10.1175/JAS-D-15-0289.1>
- Orbe, C., Yang, H., Waugh, D. W., Zeng, G., Morgenstern, O., Kinnison, D. E., et al. (2018). Large-scale tropospheric transport in the Chemistry-Climate Model Initiative (CCMI) simulations. *Atmospheric Chemistry and Physics*, *18*(7), 7217–7235. <https://doi.org/10.5194/acp-18-7217-2018>
- Pan, L. L., Atlas, E. L., Salawitch, R. J., Honomichl, S. B., Bresch, J. F., Randel, W. J., et al. (2017). The convective transport of active species in the tropics (CONTRAST) experiment. *Bulletin of the American Meteorological Society*, *98*(1), 106–128. <https://doi.org/10.1175/BAMS-D-14-00272.1>
- Pickering, K. E., Thompson, A. M., Dickerson, R. R., Luke, W. T., McNamara, D. P., Greenberg, J. P., & Zimmerman, P. R. (1990). Model calculations of tropospheric ozone production potential following observed convective events. *Journal of Geophysical Research*, *95*(D9), 14049–14062. <https://doi.org/10.1029/JD095iD09p14049>
- Ploeger, F., Abalos, M., Birner, T., Konopka, P., Legras, B., Müller, R., & Riese, M. (2015). Quantifying the effects of mixing and residual circulation on trends of stratospheric mean age of air. *Geophysical Research Letters*, *42*(6), 2047–2054. <https://doi.org/10.1002/2014GL062927>
- Podglajen, A., & Ploeger, F. (2019). Retrieving the age of air spectrum from tracers: Principle and method. *Atmospheric Chemistry and Physics*, *19*(3), 1767–1783. <https://doi.org/10.5194/acp-19-1767-2019>
- Prather, M. J., Zhu, X., Tang, Q., Hsu, J., & Neu, J. L. (2011). An atmospheric chemist in search of the tropopause. *Journal of Geophysical Research*, *116*(D4). <https://doi.org/10.1029/2010JD014939>
- Quack, B., & Wallace, D. W. R. (2003). Air sea flux of bromoform: Controls, rates, and implications. *Global Biogeochemical Cycles*, *17*(1). <https://doi.org/10.1029/2002GB001890>
- Schoeberl, M. R., Douglass, A. R., Polansky, B., Boone, C., Walker, K. A., & Bernath, P. (2005). Estimation of stratospheric age spectrum from chemical tracers. *Journal of Geophysical Research*, *110*(D21). <https://doi.org/10.1029/2005JD006125>
- Schoeberl, M. R., Douglass, A. R., Zhu, Z., & Pawson, S. (2003). A comparison of lower stratospheric age spectra derived from a general circulation model and two data assimilation systems. *Journal of Geophysical Research*, *108*(D3). <https://doi.org/10.1029/2002jd002652>
- Schoeberl, M. R., Sparling, L. C., Jackman, C. H., & Fleming, E. L. (2000). A Lagrangian view of stratospheric trace gas distributions. *Journal of Geophysical Research*, *105*(D1), 1537–1552. <https://doi.org/10.1029/1999JD900787>
- Shetter, R. E., Cinquini, L., Lefer, B. L., Hall, S. R., & Madronich, S. (2002). Comparison of airborne measured and calculated spectral actinic flux and derived photolysis frequencies during the PEM Tropics B mission. *Journal of Geophysical Research: Atmospheres*, *107*(D2). <https://doi.org/10.1029/2001JD001320>
- Singh, H. B., Salas, L., Herlth, D., Kolyer, R., Czech, E., Viezee, W., et al. (2003). In situ measurements of HCN and CH₃CN over the Pacific Ocean: Sources, sinks, and budgets. *Journal of Geophysical Research: Atmospheres*, *108*(D20). <https://doi.org/10.1029/2002JD003006>
- Smith, W. P., Pan, L. L., Honomichl, S. B., Chelpon, S. M., Ueyama, R., & Pfister, L. (2021). Diagnostics of convective transport over the Tropical Western Pacific from trajectory analyses. *Journal of Geophysical Research: Atmospheres*, *126*, e2020JD034341. <https://doi.org/10.1029/2020JD034341>
- Speight, J. G. (2017). *Environmental inorganic chemistry for engineers*. Elsevier Science.
- Stiller, G. P., von Clarmann, T., Haenel, F., Funke, B., Glatthor, N., Grabowski, U., et al. (2012). Observed temporal evolution of global mean age of stratospheric air for the 2002 to 2010 period. *Atmospheric Chemistry and Physics*, *12*(7), 3311–3331. <https://doi.org/10.5194/acp-12-3311-2012>
- Stiller, G. P., von Clarmann, T., Höpfner, M., Glatthor, N., Grabowski, U., Kellmann, S., et al. (2008). Global distribution of mean age of stratospheric air from MIPAS SF6 measurements. *Atmospheric Chemistry and Physics*, *8*(3), 677–695. <https://doi.org/10.5194/acp-8-677-2008>
- Tan, D., Faloon, I., Simpas, J. B., Brune, W., Olson, J., Crawford, J., et al. (2001). OH and H₂O in the tropical Pacific: Results from PEM-Tropics B. *Journal of Geophysical Research*, *106*(D23), 32667–32681. <https://doi.org/10.1029/2001JD900002>
- Tang, Y., Carmichael, G. R., Uno, I., Woo, J.-H., Kurata, G., Lefer, B., et al. (2003). Impacts of aerosols and clouds on photolysis frequencies and photochemistry during TRACE-P: 2. Three-dimensional study using a regional chemical transport model. *Journal of Geophysical Research*, *109*(D21). <https://doi.org/10.1029/2002JD003100>

- Waliser, D. E., & Gautier, C. (1993). A Satellite-derived Climatology of the ITCZ. *Journal of Climate*, 6(11), 2162–2174. [https://doi.org/10.1175/1520-0442\(1993\)006<2162:ASDCOT>2.0.CO;2](https://doi.org/10.1175/1520-0442(1993)006<2162:ASDCOT>2.0.CO;2)
- Wang, S., Apel, E. C., Schwantes, R. H., Bates, K. H., Jacob, D. J., Fischer, E. V., et al. (2020). Global atmospheric budget of acetone: Air-sea exchange and the contribution to hydroxyl radicals. *Journal of Geophysical Research: Atmospheres*, 125. <https://doi.org/10.1029/2020JD032553>
- Wang, S., Hornbrook, R. S., Hills, A., Emmons, L. K., Tilmes, S., Lamarque, J. F., et al. (2019). Atmospheric acetaldehyde: Importance of air-sea exchange and a missing source in the remote troposphere. *Geophysical Research Letters*, 46(10), 5601–5613. <https://doi.org/10.1029/2019GL082034>
- Wang, S., Kinnison, D., Montzka, S. A., Apel, E. C., Hornbrook, R. S., Hills, A. J., et al. (2019). Ocean biogeochemistry control on the marine emissions of brominated very short-lived ozone-depleting substances: A machine-learning approach. *Journal of Geophysical Research: Atmospheres*, 124(22), 12319–12339. <https://doi.org/10.1029/2019JD031288>
- Waugh, D. (2009). The age of stratospheric air. *Nature Geoscience*, 2, 14–16. <https://doi.org/10.1038/ngeo397>
- Waugh, D., & Hall, T. (2002). Age of stratospheric air: Theory, observations, and models. *Reviews of Geophysics*, 40(4), 1–26. <https://doi.org/10.1029/2000RG000101>
- Waugh, D. W., Crotwell, A. M., Dlugokencky, E. J., Dutton, G. S., Elkins, J. W., Hall, B. D., et al. (2013). Tropospheric SF₆: Age of air from the Northern Hemisphere midlatitude surface. *Journal of Geophysical Research: Atmospheres*, 118(19), 11429–11441. <https://doi.org/10.1002/jgrd.50848>
- Williams, M. B., Campuzano-Jost, P., Bauer, D., & Hynes, A. J. (2001). Kinetic and mechanistic studies of the OH-initiated oxidation of dimethylsulfide at low temperature—A reevaluation of the rate coefficient and branching ratio. *Chemical Physical Letters*, 344(1–2), 61–67. [https://doi.org/10.1016/S0009-2614\(01\)00764-3](https://doi.org/10.1016/S0009-2614(01)00764-3)
- Wu, Y., Orbe, C., Tilmes, S., Abalos, M., & Wang, X. (2020). Fast transport pathways into the Northern Hemisphere upper troposphere and lower stratosphere during northern summer. *Journal of Geophysical Research: Atmospheres*, 125(3). <https://doi.org/10.1029/2019JD031552>